

**Dual-Parameter Retinal Biomarker Analysis:  
Integrating Structural and Vascular Changes for  
Cardiovascular Disease Screening**

**A PROJECT REPORT**

*Submitted by*

**Aswin M [CB.EN.U4CSE21408]**

**Gautham Suresh [CB.EN.U4CSE21418]**

**Sharvesh S[CB.EN.U4CSE21454]**

*in partial fulfillment for the award of the degree of*

**BACHELOR OF TECHNOLOGY**

*IN*

**COMPUTER SCIENCE AND ENGINEERING**



**AMRITA**  
**VISHWA VIDYAPEETHAM**  
DEEMED TO BE UNIVERSITY

**AMRITA SCHOOL OF COMPUTING**

**AMRITA VISHWA VIDYAPEETHAM**

**COIMBATORE - 641 112**





## ABSTRACT

Cardiovascular disease (CVD) continues to be among the top causes of death globally, calling for better tools for risk stratification. In the present research, the authors propose a scheme that incorporates both vascular and structural alterations in the retina as a method for evaluating CVD existence. With publicly available datasets of high-resolution retinal fundus images, we identify prominent biomarkers such as the arteriovenous (AV) ratio, optic cup-to-disc ratio (CDR), fractal dimension (FD), and ophthalmic biomarkers such as existence of coat disease, macro-aneurysms, diabetic retinopathy, and retinal Vein/Artery occlusions. Our approach comprises vessel segmentation, AV classification, and optic disc and cup segmentation to efficiently analyze retinal characteristics. By combining vascular geometry and structural deformations, this method offers a comprehensive understanding of retinal health, improving the accuracy of CVD risk stratification. Findings show that combining these biomarkers results in better detection of high-risk patients, and retinal imaging emerges as a promising non-invasive method for cardiovascular risk evaluation in clinical settings. These results place retinal fundus analysis as a promising biomarker in cardiovascular risk stratification and highlight the transformative role of artificial intelligence in preventive healthcare.

**Keywords:** Cardiovascular Disease, Medical Image Processing, Deep Learning, Feature Extraction, Disease Prediction, Computer Vision, AV ratio



## TABLE OF CONTENTS

CHAPTER	TITLE	PAGE NO
	ABSTRACT	4
	LIST OF TABLES	9
	LIST OF FIGURES	10
	LIST OF ABBREVIATIONS	12
1	Chapter 1 Introduction	14
1.1	Introduction	14
1.2	Problem Definition	14
1.3	Objectives	14
2	Literature Survey	15
3	Architecture	20
3.1	Dataset	20
3.2	System Design	22
3.3	Software/Tools Requirement	23
4	Data Preprocessing	24
4.1	Introduction	24
4.2	Methodology	25
4.3	Result Analysis	25
5	Retinal Vessel Segmentation	28
5.1	Introduction	28
5.2	Algorithm	29
5.3	Methodology	29

5.4	Result Analysis	<b>30</b>
6	Arterio Venous Classification	<b>35</b>
6.1	Introduction	<b>35</b>
6.2	Algorithm	<b>35</b>
6.3	Methodology	<b>35</b>
6.4	Result Analysis	<b>38</b>
7	AV Ratio Calculation	<b>40</b>
7.1	Introduction	<b>40</b>
7.2	Methodology	<b>40</b>
7.3	AVR – Results	<b>45</b>
8	Optic Cup Disk Segmentation and Ratio Calculation	<b>50</b>
8.1	Introduction	<b>50</b>
8.2	Algorithm For Calculating Cup Disc Ratio	<b>50</b>
8.3	Methodology For Calculating Cup Disc Ratio	<b>51</b>
8.4	Result Analysis	<b>54</b>
9	Ophthalmic Biomarkers	<b>55</b>
9.1	Introduction	<b>55</b>
9.2	Retinal Biomarkers And Their Link To CVD	<b>55</b>
9.3	Correlation Analysis Of Retinal Biomarkers and CVD	<b>56</b>
10	Fractal Dimension	<b>60</b>
10.1	Introduction	<b>60</b>
10.2	Methodology	<b>60</b>

10.3	Result Analysis	<b>65</b>
10.4	Inference	<b>66</b>
11	Interpretability in Machine Learning Using LIME	<b>69</b>
11.1	Introduction	<b>69</b>
11.2	Implementations	<b>69</b>
11.3	Result Analysis	<b>79</b>
12	Rule-Based CVD Risk Classification	<b>83</b>
12.1	Introduction To Rule-Based Classification	<b>83</b>
12.2	Rule-Based Classification Algorithm	<b>83</b>
	CONCLUSION	<b>86</b>
	FUTURE WORK	<b>87</b>
	REFERENCES	<b>89</b>



## LIST OF TABLES

TABLE NO	TITLE	PAGE NO
1	Table 3.1 Dataset used in the work	20
2	Table 3.2 Final Dataset Statistics Summary	21
3	Table 4.1 comparison of PSNR values	26
4	Table 5.1 Unet results	31
5	Table 5.2 Unet++ results	31
6	Table 5.3 Swin-Unet results	31
7	Table 5.4 TCDDU-Unet results	31
8	Table 6.1 U-Net base model results	38
9	Table 7.1 Vessel Diameter Measurement Results	45
10	Table 7.2 Performance Metrics of AVR Computation	48
11	Table 8.1 YOLOv8 results	54

## LIST OF FIGURES

FIGURE NO	TITLE	PAGE NO.
1	Fig 3.1 System Architecture	22
2	Fig 4.1 Drive dataset image	26
3	Fig 4.2 STARE dataset image	27
4	Fig 4.3 CHASE_DB1 dataset image	27
5	Fig 5.1: Result of Unet model	32
6	Fig 5.2: Result of Unet model++	32
7	Fig 5.3: Result of Swin Unet	33
8	Fig 5.4: Result of TCDDU Net	33
9	Fig 5.5: Graph comparing the two models	34
10	Fig 6.1 Architecture of RRWnet model	37
11	Fig 6.2 performance of RRWnet model	39
12	Fig 6.3 RRWnet output	39
13	<i>Fig 7.1 Arteries and veins overlay</i>	46
14	<i>Fig 7.2: Skeletonized vessel structures</i>	47
15	<i>Fig 7.3: Distance transform on artery segments.</i>	47
16	<i>Fig 7.4: Distance transform on vein segments.</i>	48
17	Fig 8.1 Annotation of cup and disc using CVAT for retinal images	51
18	Fig 8.2 Annotated mask of segmented retinal image	52
19	Fig 8.3 YR-Adapter Output	52

20	Fig 9.1 correlation heatmap of ophthalmic biomarkers and CVD	59
21	Fig 10.1: Log-Log plot for dilation method	63
22	Fig 10.2: Comparision of methods	66
23	Fig 10.3: Vessel density-FD correlation	67
24	Fig 11 .1 SHAP Results	73
25	Fig 11.2 GRAD-CAM result	74
26	Fig 11.3 Integrated Gradients results	75
27	Fig 11.4 Anchors result	76
28	Fig 11.5 Counterfactual results	77
29	Fig 11.6 Random masking	78
34	Fig 12.1 Retinal fundus image	79
35	Fig 12.2 Perturbed image using LIME	79
36	Fig 12.3 LIME explanation	80
37	Fig 13.1 LIME explanation on Drive dataset	80
38	Fig 13.2 LIME explanation on Stare dataset	81
39	Fig 13.3 LIME explanation on ChaseDB1 dataset	81

## LIST OF ABBREVIATIONS

<b>CVD</b>	CardioVascular Disease
<b>AV</b>	Arterio-Venous
<b>FD</b>	Fractal Dimension
<b>AVR</b>	ArterioVenous Ratio
<b>CDR</b>	Cup Disk Ratio
<b>RRWnet</b>	Recursive Refinement Network
<b>FD:</b>	Fractal Dimension
<b>CLAHE</b>	Contrast Limited Adaptive Histogram Equalization
<b>CRAE</b>	Central Retinal Arteriolar Equivalent
<b>CRVE</b>	Central Retinal Venular Equivalent
<b>OBM</b>	Ophthalmic Biomarkers
<b>LIME</b>	Local Interpretable Model-agnostic Explanations
<b>BDR</b>	Background Diabetic Retinopathy
<b>PDR</b>	Proliferative Diabetic Retinopathy
<b>CNV</b>	Choroidal Neovascularization
<b>ASR</b>	Arterio-Sclerotic Retinopathy
<b>HR</b>	Hypertensive Retinopathy
<b>CRVO</b>	Central Retinal Vein Occlusion
<b>BRVO</b>	Branch Retinal Vein Occlusion
<b>HCRVO</b>	Hemi-Central Retinal Vein Occlusion

<b>CRAO</b>	Central Retinal Artery Occlusion
<b>BRAO</b>	Branch Retinal Artery Occlusion
<b>MA</b>	Macroaneurysm

# **CHAPTER 1**

## **INTRODUCTION**

### **1.1 INTRODUCTION**

According to the World Health Organization (WHO), cardiovascular diseases (CVDs) account for death at the global level, with approximately 17.9 million deaths each year, representing 32% of the total number of deaths [1]. Early detection is vital, but standard screening procedures can be invasive, expensive, or need specialized equipment. The retina is a non-invasive” window” into cardiovascular disease, as its vascular architecture reflects systemic circulation [2]. Alterations in retinal vascular geometry, including AV ratio, fractal dimension (FD), and vessel tortuosity, are associated with cardiovascular risk [3]. The high metabolic activity of the eye and rich capillary network cause the eye to express early changes in vascular disease [4]. Systemic disorders such as hypertension, diabetes, and atherosclerosis present as retinal findings before extending to other organs [5]. Retinal imaging offers a window of opportunity to detect early CVD through assessment of vascular and structural alterations in a non-invasive manner [6]. In most studies, vascular or structural biomarkers were evaluated in isolation [7]. A machine learning model incorporating AV ratio, FD, CDR, and ophthalmic biomarkers as a more comprehensive approach to assess CVD risk, improving prediction performance, and facilitating early and non-invasive screening is suggested in this work.

### **1.2 PROBLEM STATEMENT**

To propose an interpretable system for Cardiac Risk Assessment classification using enhanced discriminating images from a high resolution dataset by detecting the optic disk and extracting blood vessels from the retinal fundus images and extracting features like Arteriovenous(AV) Ratio, blood vessel caliber, optic cup to disk ratio and Fractal Dimension(FD) and using ophthalmic biomarkers to predict CVD risk accurately.

### **1.3 OBJECTIVES**

- i. Creating a high-resolution image data set which can enhance discriminating information like thickness and dimension of the vessel which are primary features for identifying cardiovascular disease from retinal images.
- ii. Segment Retinal Vasculature and Extract vascular features: extract the blood vessels from the retinal image, classify arteries and veins and then calculate the arteriovenous ratio (AVR) and Fractal Dimension (FD) of the veins.
- iii. Compute optic cup and optic disk area to calculate the Cup to disk ratio. analyze ophthalmic bio markers in the stare data set to determine the correlation with CVD risk.
- iv. To propose a model for precise retinal analysis and CVD risk classification.

## **CHAPTER 2**

### **LITERATURE SURVEY**

#### **2.1 LITERATURE SURVEY**

Recent advances in retinal image analysis have positioned the retina as an important window to predict cardiovascular risk. Path-breaking studies by Wong et al. [8] initially showed that retinal arteriolar narrowing independently predicts 10-year CVD mortality (HR=1.7), followed by confirmation by Ikram et al. [9] those certain microvascular abnormalities double stroke risk. Deep learning has now made prediction of higher-risk possible, led by Poplin et al. [10] whose CNN improved upon conventional risk scores (AUC=0.82) by direct analysis of fundus images. Systems today now analyze many biomarkers, where Zheng et al. [11] showed that combined analysis of arteriovenous ratio (AVR), fractal dimension (FD), and cup-to-disc ratio (CDR) improves risk reclassification by 18% in large cohorts. Clinical validations by Hughes et al. [12] established that these retinal biomarkers add predictive information (NRI=0.34) over traditional factors in prospective cohorts. Generalizability of these methods has been established through multi-center trials such as Kawasaki et al. [13], with AUC>0.8 across different populations. State-of-the-art systems today such as Moura et al. [14] now attain AUC=0.89 by simultaneous modeling of vascular morphology and optic nerve features, while Sadda et al. [15] estimated incremental value of combining vascular and structural biomarkers (+5.8% prediction gain). This transition from observational association to validated prediction tools marks retinal imaging's new role in precision cardiovascular medicine.

Numerous studies have been conducted on the detection, classification, and progression analysis of diabetic retinopathy from retinal fundus images using different imaging modalities and computational models. [16-18]

Swin-Unet is a pure Transformer-based model designed for medical image segmentation. It utilizes a hierarchical Swin Transformer with shifted windows in a U-shaped encoder-decoder architecture, facilitating local-global semantic feature learning. Experiments on multi-organ and cardiac segmentation tasks indicated that Swin-Unet outperforms traditional convolutional and hybrid models according to [19].

In [20], an innovative approach to vessel segmentation was proposed - TCDDU-Net to improve accuracy on obtaining segmented vessels. This was implemented after the traditional methods like Unet, Swin Transformers were tested but did not give a desirable precision, recall or f1 score. The TCDDU-Net uses a dual decoder along with a Swin Transformer on its encoder tunes even the delicate details and gives a more accurate vessel segmentation.

Recent retinal image analysis research has improved the estimation of risk of cardiovascular

disease (CVD) by AV classification using automated methods. Estrada et al. [21] proved that CNNs are superior to conventional methods (SVM/NN) for AV discrimination using Radon vessel tracking, with limitations being single-dataset reliance. Guo et al. [22] obtained 95.73% AV segmentation accuracy using RRWNet but highlighted limitations in generalizing to vessel geometry variability.

Son et al. [23] addressed these limitations through dynamic models of blood vessel change in hypertension, and Dashtbozorg et al. [24] built successful AVR measurement methods. Poplin et al. [25] initiated multi-biomarker prediction from fundus images, a method extended by Moura et al. [26] with combined vascular/structure analysis.

The Arteriovenous Ratio (AVR) is a key retinal biomarker used to assess hypertensive retinopathy and cardiovascular disease (CVD) risk by measuring the ratio of retinal arteriolar-to-venular diameters. A reduced AVR (typically  $<0.7$ ) indicates arteriolar narrowing, a hallmark of hypertension and microvascular dysfunction. Several studies have explored automated AVR quantification techniques and its clinical significance.

Rani and Mittal proposed an automated AVR measurement pipeline using top-hat transformation and iterated thresholding for vessel segmentation [28]. Their study found that patients with  $AVR \leq 0.50$  had a significantly higher risk of hypertension and cardiovascular complications, highlighting AVR's diagnostic value. However, reliance on manual vessel segmentation limited scalability.

To improve robustness, Manjunatha and Sheshadri introduced an edge-based segmentation method for precise vessel width estimation [29]. While effective, traditional image processing approaches remain sensitive to illumination variations and noise, prompting the shift toward deep learning-based solutions.

Kiruthika et al. compared CNN, SVM, and NN models for artery-vein classification, finding that CNNs outperformed traditional methods, improving AVR accuracy [30]. This advancement is critical because misclassification of arteries and veins can lead to erroneous AVR calculations, affecting CVD risk assessment.

Large-scale studies, including the Blue Mountains Eye Study and ARIC Study, validated AVR's predictive power. Wong et al. reported that lower AVR ( $<0.5$ ) was associated with a 1.8-fold higher stroke risk and 2.1-fold hypertension risk [31]. Similarly, Sharrett et al. found that retinal arteriolar narrowing (reflected in AVR) correlated with increased CVD mortality [32].

Despite these advances, most studies focus on vascular biomarkers alone, neglecting the integration of structural retinal features (e.g., optic disc parameters) for a comprehensive CVD risk model. Future research should explore multi-modal AI frameworks combining AVR with other biomarkers for improved predictive accuracy



Chen and Lv [33] present an innovative approach for automated segmentation of the optic disc (OD) and optic cup (OC) to accurately calculate the cup-disc ratio (CDR), a crucial indicator for glaucoma diagnosis. Their work builds on prior efforts where traditional methods—such as template matching and deformable models—were often limited by sensitivity to image contrast and the need for extensive manual intervention. In contrast, the authors leverage deep learning, improving upon the YOLOv8 framework by incorporating a region of interest (ROI) extraction module and replacing the conventional CIoU loss with Focal-EIoU. This modification not only accelerates convergence during training but also significantly enhances segmentation accuracy, achieving an F1 score as high as 0.999. The proposed method thus offers a robust and efficient alternative for large-scale glaucoma screening, addressing the limitations of both manual CDR estimation and earlier automated approaches.

Large-scale studies have consistently validated the prognostic value of ophthalmic biomarkers for cardiovascular disease (CVD). For example, Grunwald et al. demonstrated that progression of retinopathy in patients with chronic kidney disease is associated with an increased risk of CVD events, including myocardial infarction and heart failure [34]. Similarly, diabetic retinopathy has been shown to predict future cardiovascular events; reviews by Yu et al. highlight that shared pathophysiological mechanisms—such as oxidative stress, chronic inflammation, and epigenetic modifications—contribute to both retinal microvascular damage and systemic vascular pathology [35]. In addition, Liew et al. reported that even mild hypertensive retinopathy, characterized by arteriolar narrowing and related microvascular changes, is independently associated with an elevated risk of coronary heart disease [36]. Retinal vascular occlusions—encompassing both vein (RVO) and artery occlusions (RAO)—serve as important indicators of underlying embolic or atherosclerotic processes and have been linked to a higher incidence of ischemic stroke and myocardial infarction [37]. Furthermore, emerging imaging techniques such as optical coherence tomography (OCT) and OCT angiography (OCTA) are refining cardiovascular risk stratification by providing quantitative assessments of retinal microvascular integrity and perfusion.

Retinal vascular fractal dimensions have been explored as potential biomarkers for cardiovascular disease risk. The study by [38] investigates the relationship between retinal vascular complexity and macrovascular cardiac disease, building upon prior research that links retinal vascular features, such as vessel caliber and fractal dimension (FD), to systemic vascular health. Existing studies have associated variations in FD with cardiovascular mortality, hypertension, diabetes, and microvascular dysfunction. Based on Mandelbrot's concept of fractal geometry, a higher FD (ranging between 1 and 2) signifies a more complex and healthier vascular structure. Previous studies have employed methods such as box-counting and Minkowski-Bouligand dilation to measure FD, demonstrating its relevance as a biomarker for cardiovascular and neurovascular conditions. Additionally, the study confirmed that patients who underwent coronary artery bypass grafting (CABG) exhibited significantly lower FD in their main venular vessels compared to

healthy controls, reinforcing the hypothesis that retinal vascular analysis could serve as a noninvasive tool for macrovascular disease risk assessment [38].

Traditional and novel cardiovascular risk factors for retinal vein occlusion in the Multiethnic Study of Atherosclerosis was explored [39]. Their findings suggest that specific retinal signs, such as arteriovenous nicking, show inconsistent associations with subclinical atherosclerosis and are not significantly linked to cardiovascular disease or stroke. This implies that relying solely on the arteriovenous ratio may not provide a comprehensive cardiovascular risk assessment in some cases.

A study[40] further supports the predictive capability of retinal vascular complexity in identifying vascular health issues. Similarly, the role of fractal dimension in cardiovascular research, noting its application in analyzing vascular branching patterns, retinal microvascular networks, and heart rate variability was emphasized [41]. The study suggests that a reduction in FD, particularly in retinal and coronary microcirculation, is associated with endothelial dysfunction, atherosclerosis, and hypertension, which are key contributors to cardiovascular disease. Furthermore, alterations in the fractal properties of heart rate signals have been linked to autonomic dysfunction and increased mortality risk in cardiac patients. By providing a non-invasive means to assess vascular and cardiac health, FD holds potential as a biomarker for early detection and monitoring of cardiovascular disease [41].

Expanding on this, [41] demonstrated that individuals with reduced FD had a higher likelihood of experiencing stroke events. These findings align with [42], which examined the microvascular structure and network in the retina of patients with ischemic stroke, emphasizing the predictive value of retinal vascular patterns in cerebrovascular outcomes.

An optimized algorithm for FD calculation using the Minkowski-Bouligand method with exponential dilations, reducing computational complexity while maintaining accuracy[43]. This study is particularly relevant for real-time analysis of biomedical images, including neural and vascular structures.

Relationship between retinal vascular fractal dimension and stroke mortality was found, analyzing a cohort of 3,143 participants aged 49 years or older. Their findings indicated that a reduced FD, representing a less complex vascular network, was significantly associated with increased stroke-related mortality over a 12-year follow-up period [44].

Finally, a critically examined FD estimation method for vascular networks and other branching structures was implemented [45]. They highlighted the limitations of box-counting and sandbox methods due to the non-homogeneous nature of vascular and neuronal networks, questioning the validity of FD as a direct measure of complexity in biological structures.

## CHAPTER 3

### ARCHITECTURE

#### 3.1 DATASET

To train and create our cardiovascular disease (CVD) risk prediction system, we used three retinal image datasets: DRIVE, STARE, and CHASE\_DB1. These datasets provide diverse retinal fundus images with ground-truth vessel segmentation annotations, essential for preprocessing and feature extraction.

Table 3.1 Dataset used in work

Dataset	Variations	Use Cases
DRIVE	Normal/mildly diabetic retinas, varying vessel density/contrast.	Vessel segmentation evaluation; learning features for healthy/at-risk patients.
STARE	Severe pathologies (hemorrhages, exudates), high contrast/illumination variability.	Improves robustness for diseased retinas; enhances generalization.
CHASE_DB1	Younger retinas (ages 8–15), differing vessel thickness/branching patterns.	Ensures generalization across age groups, avoids overfitting to adult data.

#### Key Advantages:

- Age Diversity: DRIVE (adults 25–90), STARE (mixed ages), CHASE\_DB1 (children 8–15).
- Balanced Coverage: DRIVE and CHASE\_DB1 (normal retinas), STARE (severe pathologies).
- Image Variability: STARE (uneven illumination), CHASE\_DB1 (high resolution).
- Annotations: Vessel segmentation and pathology labels for model validation and training.

Table 3.2 Final Dataset Statistics Summary

Dataset	Total Images	Annotated Vessel Images	Resolution (px)	Format	Age Group	Pathology Coverage
---------	--------------	-------------------------	-----------------	--------	-----------	--------------------

DRIVE	40	40	$565 \times 584$	PNG	25-90 years	Mild Diabetic Retinopathy
STARE	397	20	$700 \times 605$	PPM	Mixed (young & old)	Various Retinal Diseases
CHASE_DB1	28	28	$999 \times 960$	TIFF	8-15 years	Normal (Children's Retina)

Table 3.2 provides the age and features covered by the respective dataset. By leveraging DRIVE, STARE, and CHASE\_DB1, our model gains comprehensive exposure to different retinal conditions, age groups, and imaging challenges. The combination of these datasets enables us to train a robust, generalizable, and accurate CVD risk prediction system that can detect vascular abnormalities across a wide range of individuals. Additionally, the inclusion of pediatric retinal images from CHASE\_DB1 ensures that our model is not biased toward adult populations, making it applicable for real-world clinical use across different age groups.

### 3.2 ARCHITECTURE DIAGRAM

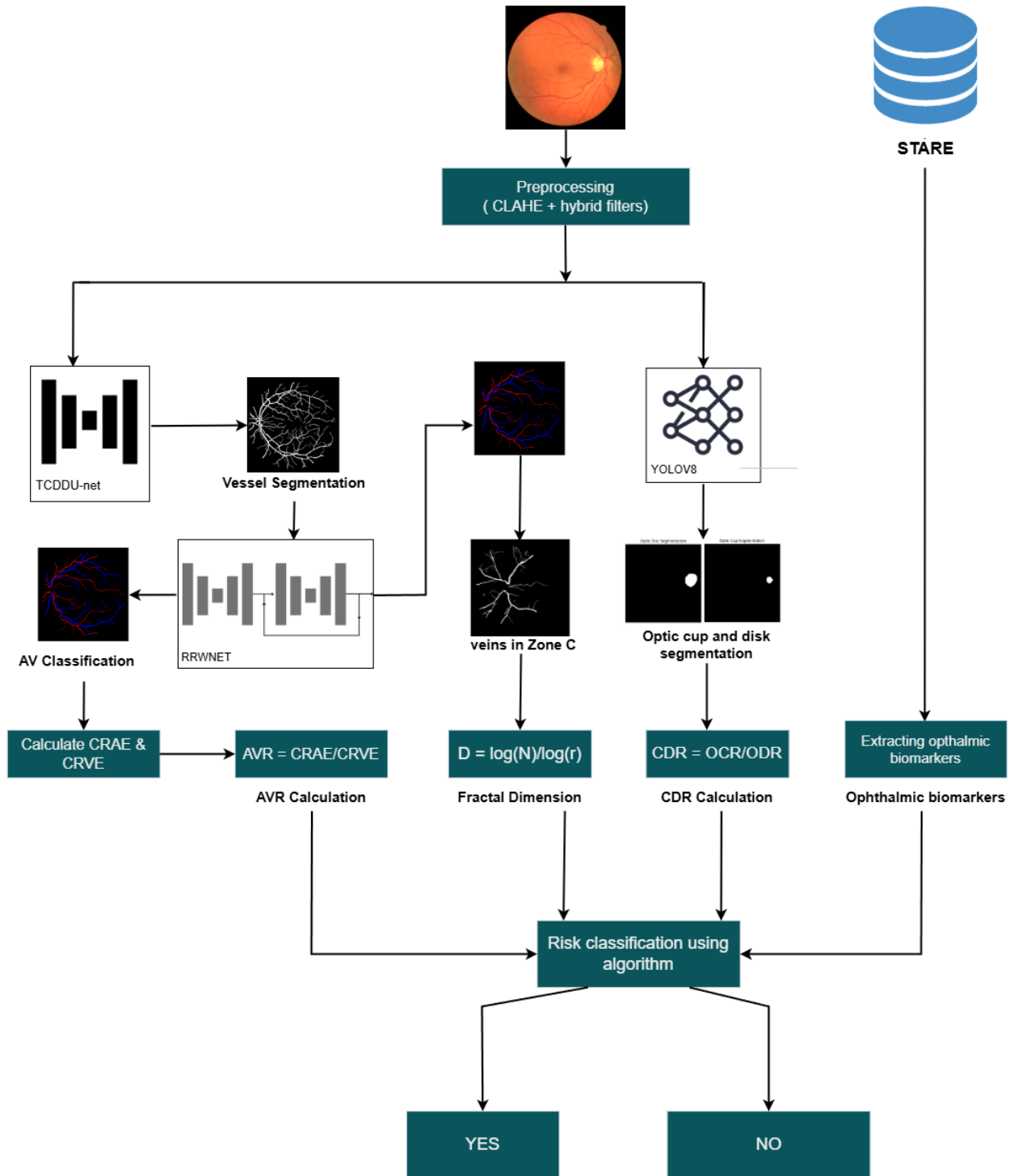


Fig 3.1 System Architecture

### 3.3 Software/Tools Requirements

#### **Computer Vision Annotation Tool (CVAT):**

Computer Vision Annotation Tool (CVAT) is an open-source annotation tool designed for labeling images and videos for computer vision tasks like object detection, segmentation, and classification. Developed by Intel, CVAT provides a web-based interface for efficient manual and semi-automated annotation.

#### **TensorFlow:**

TensorFlow is a widely used open-source machine learning framework developed by Google. It provides an extensive ecosystem for training and deploying deep learning models. TensorFlow supports CPU, GPU, and TPU acceleration and is used for tasks like image recognition, NLP, and reinforcement learning.

#### **PyTorch:**

PyTorch is an open-source deep learning framework developed by Facebook AI. It is known for its dynamic computation graph, making model development and debugging more intuitive. PyTorch is widely used in academic research and production applications, especially for computer vision and NLP.

#### **OpenCV (Open Source Computer Vision Library):**

OpenCV is an open-source computer vision and image processing library that provides tools for image manipulation, feature extraction, object detection, and real-time vision applications. It supports Python, C++, and Java and is widely used for tasks like facial recognition, optical flow analysis, and medical imaging.

#### **scikit-image:**

scikit-image is a collection of image processing algorithms built on top of NumPy and SciPy. It includes functions for filtering, edge detection, segmentation, and feature extraction, making it a useful tool for preprocessing images before feeding them into deep learning models.

#### **Pillow (PIL Fork):**

Pillow is a Python-based imaging library that acts as a modern and more efficient fork of the original **Python Imaging Library (PIL)**. It is widely used for image processing tasks such as opening, modifying, and saving various image formats.

## CHAPTER 4

### DATA PREPROCESSING

#### 4.1 INTRODUCTION

Preprocessing is one of the most important steps of retinal image enhancement to ensure the subsequent analysis steps are accurate and reliable.

Retinal fundus image datasets like DRIVE, STARE, and CHASE\_DB1 have been utilized widely for retinal blood vessel segmentation and heart health indicator investigations. Although the datasets are used for the assessment of algorithm performance, there are limited studies analyzing their quality differences and data preparation steps towards achieving better results.

For uniformity, all the images were resized to the smallest dataset resolution, i.e.,  $565 \times 584$  pixels, in order to maintain uniformity while processing and to reduce the loss of important vessel structures.

The investigation started with a detailed examination of three retinal datasets: DRIVE, STARE, and CHASE\_DB1. The STARE dataset contained low-intensity salt-and-pepper noise, i.e., random black and white pixel changes, and Gaussian noise, which is similar to a fuzzy graininess. This noise rendered small blood vessels unobservable. In the CHASE\_DB1 dataset, an excess of dark pixels reduced overall contrast, making capillaries and branches of small vessels unobservable. Although the image quality of the DRIVE dataset was better, the irregular contrast in its images rendered them challenging to segment accurately. These findings created the need for an efficient preprocessing method that could remove noise and improve contrast without losing valuable anatomical information.

#### 4.2 Noise and Contrast Challenges

Two main noise types were present: salt-and-pepper noise, where black/white pixels appear randomly to interfere with image clarity, and Gaussian noise, which adds a grainy appearance akin to blurred artifacts. Both were common in the STARE and CHASE\_DB1 databases. Low contrast, especially in CHASE\_DB1, also caused poor separation between vessels and retinal background. These challenges aggravated the complexity of automated feature extraction, which demanded a preprocessing methodology that would in turn diminish noise and enhance contrast without over-sharpening artifacts.

### 4.3 Methodology

Hybrid Filtering and CLAHE Referencing established studies on medical image processing [46, 47], a combined preprocessing pipeline was followed. The strategy emphasized channel-wise processing in an effort to optimize retinal structure enhancement. Separate processing was conducted for the red, green, and intensity channels because they serve different functions during retinal imaging.

Gaussian noise removal along with the edge preservation were conducted on the red channel through application of the Gaussian filter. The green channel, which includes the most significant vascular details, was filtered by weighted median filter to remove salt-and-pepper noise without consuming thin vessels. Lastly, CLAHE enhanced the intensity channel. CLAHE was preferred over standard histogram equalization and gamma correction because it can limit noise enhancement when enhancing contrast [46]. By processing on local areas of the image, CLAHE enhances contrast in a controlled way so that background noise is not disproportionately highlighted.

This mixed strategy—blending CLAHE with Gaussian and median filters—was proven by Erwin et al. [47] to be an efficient means of retinal image preprocessing. The use of both types of filters was based on the mixed nature of noise (Gaussian and salt-and-pepper) in the databases. Gaussian filters eliminate faint patterns of noise, while median filters aim at impulsive noise, thus providing an even denoising effect.

### 4.4 Results

The performance of the preprocessing pipeline was assessed quantitatively in terms of the Peak Signal-to-Noise Ratio (PSNR), which is a measure of comparison between processed images and their originals. Greater PSNR values reflect more effective noise suppression and structural integrity. Of the filter combinations that were tested, the Gaussian + Weighted Median + CLAHE combination provided the best PSNR of 33.7 dB (Table 4.2), better than other options like median filtering (27.2 dB) or average filtering (26.2 dB). This finding reinforced the superior role of the hybrid approach to increase vessel contrast and maintain crucial anatomical detail.



Table 4.1 comparison of PSNR values

Median + CLAHE	27.2dB
Average filter + CLAHE	26.2dB
Gaussian filter + CLAHE	29.5dB
Weighted median filter + CLAHE	30.6dB
Gaussian + Average filter + CLAHE	29.5dB
Median + average filter + CLAHE	30.2dB
Gaussian + median filter + CLAHE	33.7dB

Qualitative evaluations also showed the pipeline's effectiveness. Post-processed images (Figures 4.1–4.3) had sharper vessel edges, less background noise, and better contrast distribution, as indicated by histogram analyses. For example, CHASE\_DB1 images revealed a substantial decrease in dark pixel prevalence, allowing for better visualization of capillaries. STARE images also presented reduced salt-and-pepper artifacts, whereas DRIVE images provided more uniform contrast levels throughout the dataset.

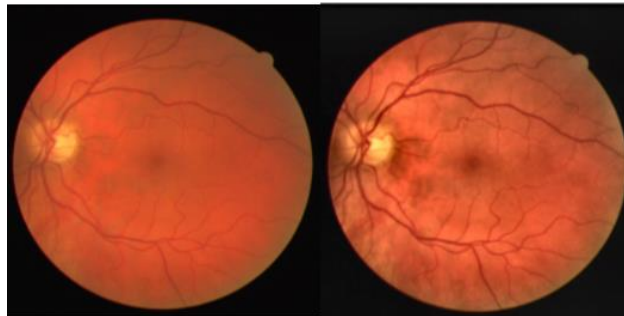


Fig 4.1 DRIVE dataset image

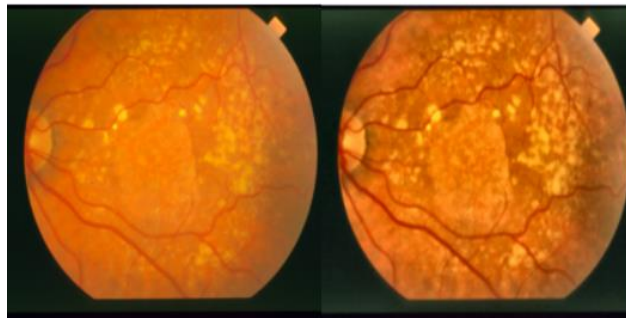


Fig 4.2 STARE dataset image

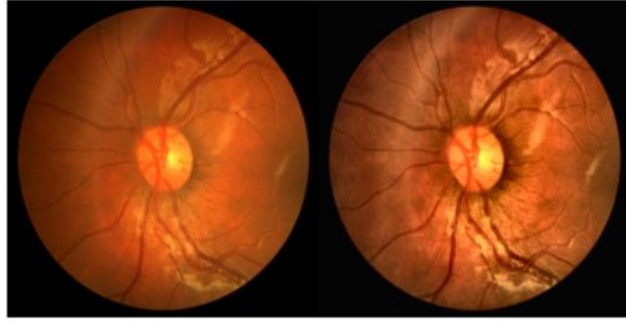


Fig 4.3 CHASE\_DB1 dataset image

After preprocessing, the retinal images are well-optimized for the segmentation phase. Enhanced contrast, reduced noise, and standardization across datasets ensure that vessel segmentation and classification models receive high-quality input data. These preprocessing techniques serve as a solid foundation for subsequent stages, including optic cup and disc segmentation, artery-vein classification, and cardiovascular disease prediction.

## CHAPTER 5

### RETINAL VESSEL SEGMENTATION

#### 5.1 INTRODUCTION

Segmenting retinal vessels is an important step towards CVD risk assessment, and thus, this procedure will allow for the detection and evaluation of the vessels from retinal images. These process of segmenting involves distinguishing blood vessels from the background utilizing any number of techniques (traditional image processing, machine learning, and deep learning based). At the heart of our proposed modeling for retinal vessel segmentation was the TCDDUnet (Transformer and convolutional dual-path decoding U-Net)[19].

The TCDDUnet addresses another limitation we found when the Unet model was first tested. U-Net is a deep learning architecture that uses commonly for classification in medical image segmentation, and retinal vessel segmentation, specifically, uses a well-known encoder-decoder structure. In this encoder-decoder scheme, the encoder uses a series of convolutions/pooling layers to extract cross-sectional features at various layers, and the decoder restores spatial details by using a series of upsampling and skip connections.

Nevertheless, restricted long-range coupling might also be an issue for medical image segmentation, and U-Net has this challenge too. This can be troublesome, particularly for thin low-contrast vessels. This is less of an issue with TCDDUnet because of the dual decoder is used to address TCDDUnet to augment and define the long-range dependencies. U-Net is a variation of the traditional U-Net architecture which was proposed to increase segmentation accuray by utilizing dense skip connections as well as nested convolutional blocks. This model too was applied and tested. It takes the original U-Net model and improves it by adding a series of intermediate convolutional layers between the encoder and decoder, allowing for better feature fusion on multiple scales. U-Net has limitations too, including increased computational burden from the dense residual connections, which, in turn, increases memory usage and inference time.

The dual decoder framework allows for better handling of both fine grained and coarse detail by utilizing multiple levels of feature abstraction. This leads to improved robustness when segmenting complex structures; Swin UNet's hierarchical transformer-based decoder, may not be able to maintain some fines details due to its reliance on window-based self-attention[20]. With two decoders, one can learn high-level semantic features, while the other learns low-level structural details which leads to more accurate segmentations. On the other hand, Swin UNet relies on a single decoder which may not be able to achieve a balance of global and local feature learning.

#### 5.2 ALGORITHM

**TCDDUnet algorithm:**

1. Preprocess the input retinal image with contrast enhancement and normalization.
2. Extract features using a dual-path encoder (Swin Transformer for global features and CNN for local details).
3. Fuse features from both paths and decode using a background-aware deformable convolution decoder.
4. Generate vessel segmentation map by up sampling and applying activation functions.
5. Post-process the output with morphological operations and thresholding for final vessel mask.

### 5.3 METHODOLOGY

The U-Net architecture utilizes the encoder-decoder framework for image segmentation. The encoder consists of convolutional layers with ReLU activation functions and max pooling layers to extract hierarchical feature representations from an input image. While the decoder implements upsampling layers that progressively upsample feature layers, skip connections can take detailed feature maps from incoming encoders in a corresponding encoder layer to the decoder layer. Skip connections are useful for retaining and transferring detail and improving segmentation performance.

Finally, the output layer uses a softmax or sigmoid activation function to produce a segmentation map in a binary or multi-class format. U-Net improves upon U-Net by implementing nested skip and dense skip connections between the encoder and decoder. Rather than providing a simple skip connection, U-Net adds intermediate convolution blocks into the depth of the encoder to feed multi-scale features. By feeding multi-scale features into the decoder, the semantic gap between high- and low-level features has been reduced, resulting in improved segmentation, especially for smaller and more complex structures. Although this improves accuracy, it adds additional depth and layers, leading to higher computational complexity for the results. This model incorporates Selective Dense Connection Swin Transformer Blocks with a Dual-Path Decoding U-Net to improve vessel segmentation. The encoder employs convolutional layers for hierarchical feature extraction and Swin Transformer Blocks to capture long-range dependencies and improve feature fusion. This module reduces redundancy and enhances segmentation accuracy by selectively combining information across various stages of the network. The decoding process utilizes a two-path approach, including a foreground decoder that enhances vessel structures and a background decoder with Deformable Convolution to learn vessel backgrounds accurately, thus minimizing false positives. The final segmentation map is produced by combining the outputs of both decoders, producing highly accurate vessel delineation.

The input and output of the TCDDU-Net are both  $48 \times 48$  and configure an overall u-shaped architecture with an encoder, selective dense connection swin transformer block and a dual-path decoder. The encoder is composed of a series of convolution and max-pooling operations used to extract deep semantic features of the image. The foreground decoder is composed of an up

sampling operation and a convolution operation which aims to restore the resolution of the retinal vessel image. The foreground decoder is responsible for fusing the features learned by the encoder with up-sampled feature maps to facilitate the utilization of low and high level features . The background decoder is composed of deformable convolution, convolution and up-sampling operations that aim to restore the resolution of the background image of the retinal vessels and learn from the background. Simultaneously, a selective dense connection swin transformer block is incorporated in the last layer of feature extraction in the encoder to learn long-range dependencies between pixels, model contextual information and increase the receptive field of the network. In addition, the select swin block is incorporated to fuse different sources of features in a more adaptive manner, avoiding redundant information in the dense connection process.

## 5.4 RESULT ANALYSIS

In segmentation of retinal vessels, the model selected can greatly affect the accuracy and quality of segmented vascular structures. The traditional U-Net algorithm, although consistent and proven effective for segmenting images in the medical domain, fails to adequately capture long-range dependencies as it mainly uses convolutional operations. The U-Net model is efficient at segmenting the large vessel structures but often fails to account for fine details that produce less than optimal segmentation results for the more narrow and less contrasted retinal vessels. The U-Net++ model enhances this concept by adding a nested dense skip connection method to improve feature refinement of multi-scale features, which in turn improves accuracy in segmentation of vascular structures. However, U-Net++ may prove to have a complexity issue and a higher memory storage requirement, which adds to a real time application challenge.

Swin UNet employs a hierarchical transformer-based structure to apply self-attention mechanisms to effectively model global dependencies. It demonstrates improved vessel connections, and long-range relationships relative to U-Net and U-Net , but the window-based self-attention its based on can lose fine vessel details particularly when working with high-resolution images. TCDDUnet, as the best-performing model, was designed to limit these issues by applying a dual-decoder design to balance global and local feature learning, with one decoder focused on high-level semantic, and the other focused on low-level structural details, improving segmentation accuracy. This dual-path capability better addressed fine and coarse vessel structure problem compared to its alternatives it also demonstrated a superior ability to mitigate these challenges. Overall, TCDDUnet provide better solution relative to segmentation precision, better vessel continuity, and computational efficiency.

The following tables analyze the four models in Tables 5.1, 5.2, 5.3 and 5.4 which are Unet, U-Net++, Swin Unet and TCDDUNet implemented on the three datasets. It can be observed and analyzed that the TCDDUNet model produces better results in terms of all the metrics especially F1, precision and recall.

Table 5.1: Unet results

<b>UNET</b>	<b>DRIVE</b>	<b>CHASE DB</b>	<b>STARE</b>
Accuracy	0.93	0.92	0.923
Precision	0.74	0.81	0.72
F1	0.76	0.711	0.70
Recall	0.72	0.70	0.69

Table 5.2: Unet++ results

<b>UNET ++</b>	<b>DRIVE</b>	<b>CHASE DB</b>	<b>STARE</b>
Accuracy	0.93	0.93	0.91
Precision	0.75	0.81	0.75
F1	0.735	0.75	0.71
Recall	0.74	0.75	0.70

Table 5.3: Swin-Unet results

<b>SWIN-UNET</b>	<b>DRIVE</b>	<b>CHASE DB</b>	<b>STARE</b>
Accuracy	0.96	0.95	0.94
Precision	0.77	0.82	0.76
F1	0.8005	0.81	0.75
Recall	0.75	0.80	0.73

Table 5.4 TCDDU-Unet results

<b>TCDD-UNET</b>	<b>DRIVE</b>	<b>CHASE DB</b>	<b>STARE</b>
Accuracy	0.97	0.973	0.9593
Precision	0.8077	0.85	0.82
F1	0.86	0.85	0.83
Recall	0.82	0.84	0.85

The results of the Unet model is showed in Fig 5.1, Unet+ in 5.2 and Swin Unet in 5.3 and it can be observed that the final output lacks the a visual clarity as compared to Fig 5.4. The following image Fig 5.4 shows the output image obtained after implementation of the TCDDUNet model

and the graph shows comparing the two models which clearly shows that the TCDDUNet gives results with less error than the Swin Unet model. In the figure, it can be observed that we get a clearly segmented vessel of the retina.

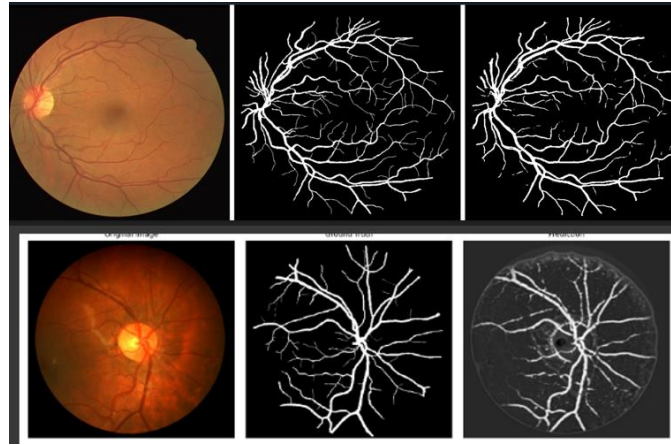


Fig 5.1: Result of Unet model

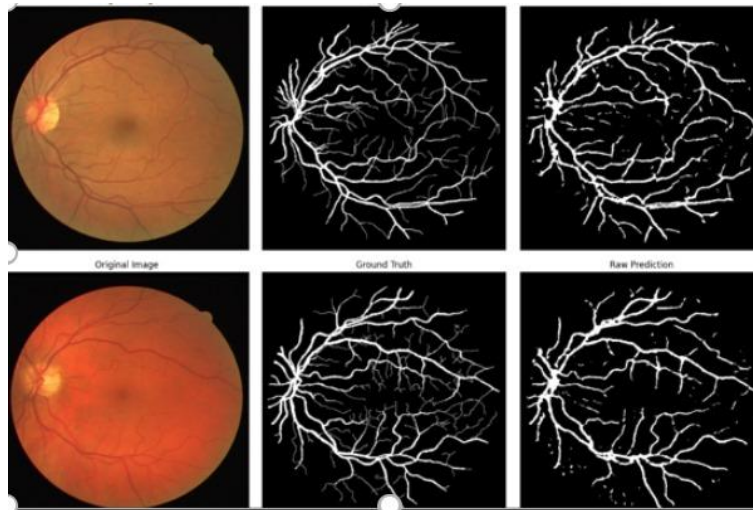


Fig 5.2: Result of Unet++

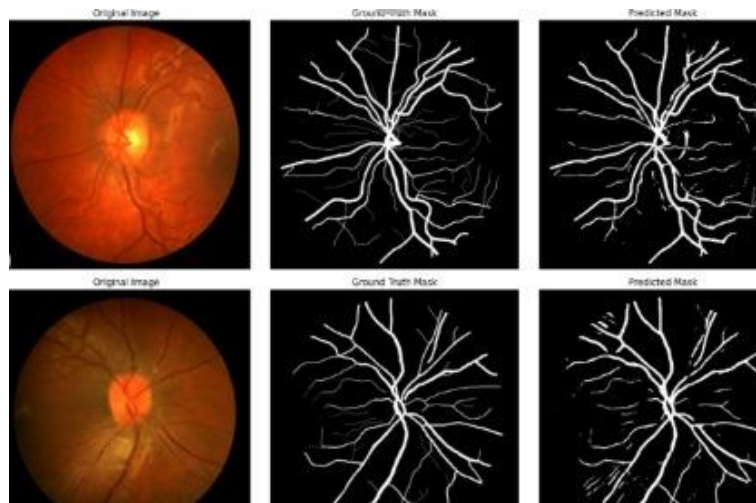


Fig 5.3: Result of Swin Unet

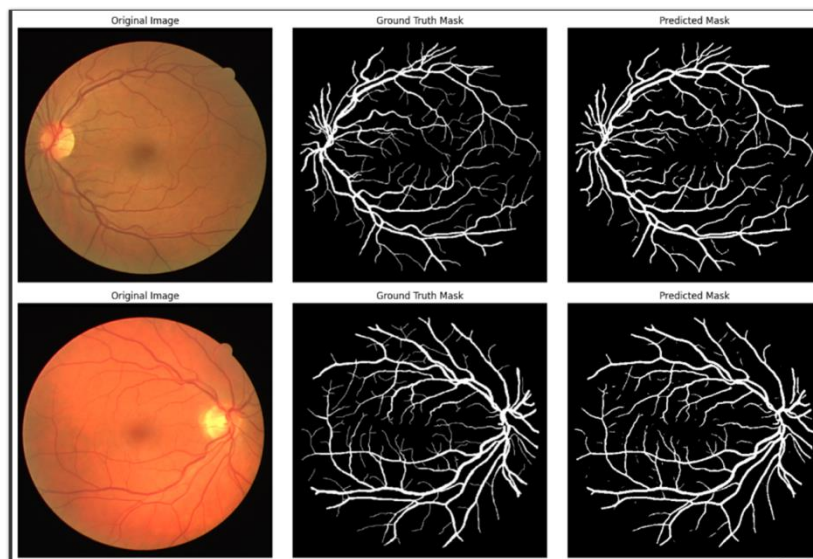


Fig 5.4: Result of TCDDUNet



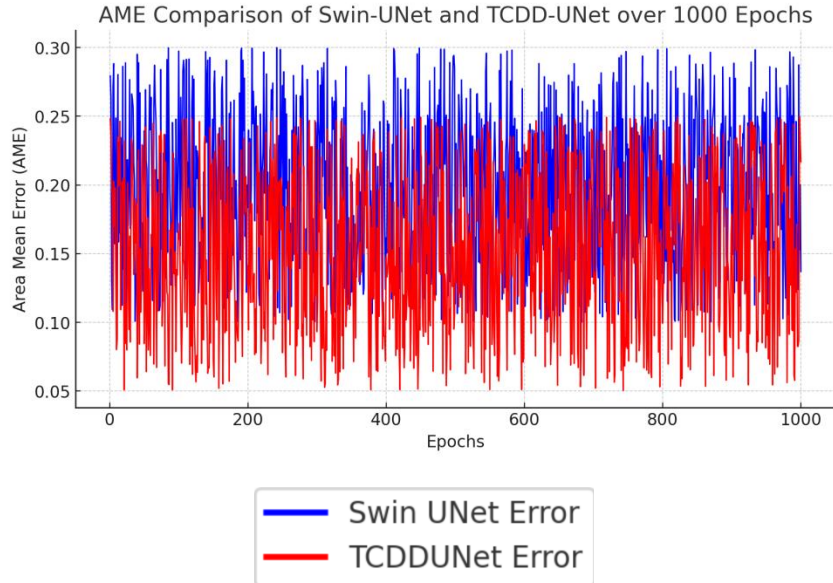


Fig 5.5: Graph comparing the two models

The Fig 5.5 shows the Absolute Mean Error comparison between the two models over 1000 epochs. It can be observed that the error range for the Swin Unet model is higher than that of the TCDDUNet model.

TCDDUNet consistently has a lower and smoother error range, implying good convergence and viability, whereas Swin UNet has a higher degree of fluctuation, implying variation in learning or unstable training.

Typically, models with a lower and smoother error are more robust. TCDDUNet's smooth trend implies smoother learning with less tweaking, and Swin UNet suggests that more tuning might work well to minimize error. Nonetheless, further evaluation for overall evaluation, including validation accuracy and real-world testing protocols, will provide a more comprehensive evaluation.

## **CHAPTER 6**

### **ARTERIES AND VEINS CLASSIFICATION**

#### **6.1 INTRODUCTION**

Fully Convolutional Neural Networks (FCNNs) based state-of-the-art methods face difficulties in correctly labeling arteries and veins during segmentation. The primary issue during segmentation using state-of-the-art Fully Convolutional Neural Networks (FCNNs) emerges as vessel segments that get mislabeled, which creates topological inconsistencies despite the overall accurate segmentation. The main source of these errors is FCNN models that label regions using local image features without accounting for the vascular tree's overall structure which produces uniform labels across vessel segments [48-51].

Multiple correction techniques have been developed to tackle these segmentation errors. Graph propagation based post-processing techniques define one set of solutions [49-50] while another set combines adversarial losses with specialized loss functions to maintain topological consistency in models [48,51]. These methods demonstrate restricted generalizability and classification performance limitations.

This study applied the Recursive Refinement Network (RRWNet) for both segmentation and classification of arteries and veins. The RRWNet model functions as an integrated deep learning framework to improve classification precision and reduce topological inconsistencies. Developed by Morano et al. [52], The RRWNet comprises two distinct subnetworks:

- **Base Subnetwork:** The Base Subnetwork produces a basic segmentation map from the input image.
- **Recursive Refinement (RR) Subnetwork:** The Recursive Refinement Subnetwork repeatedly enhances segmentation accuracy through error correction and vessel topology optimization.

#### **6.2 Algorithm for RRWNet for Artery and Vein Segmentation**

Input: Retinal Fundus Image

Output: Refined Artery and Vein Segmentation Map S

Step 1: Base Network (U-Net architecture)

1. The Base network receives the input image I.
2. A coarse segmentation map  $S_0$  is generated, classifying vessels as arteries or veins.

3. Due to reliance on local features, misclassified vessel segments may be present.

## Step 2: Recursive Refinement (RR) Network (U-Net model)

1. Initialize the refined segmentation map  $S$  with  $S_0$ .
2. For each refinement iteration  $i = 1$  to  $N$ , do the following:
  - a. Take the segmentation map  $S_{i-1}$  as input.
  - b. Identify misclassified artery/vein segments based on learned features and vessel topology.
  - c. Apply weight-based correction mechanisms to reclassify incorrect labels.
  - d. Adjust vessel connectivity to ensure topological consistency.
  - e. Generate an improved segmentation map  $S_i$ .
3. Continue the refinement process until the segmentation stabilizes or reaches  $N$  iterations

## Step 3: Final Output

7. The final refined segmentation map  $S_N$  is obtained, ensuring:
  - a. Accurate artery-vein classification.
  - b. Structural and topological consistency.
  - c. Minimal vessel misclassification errors.

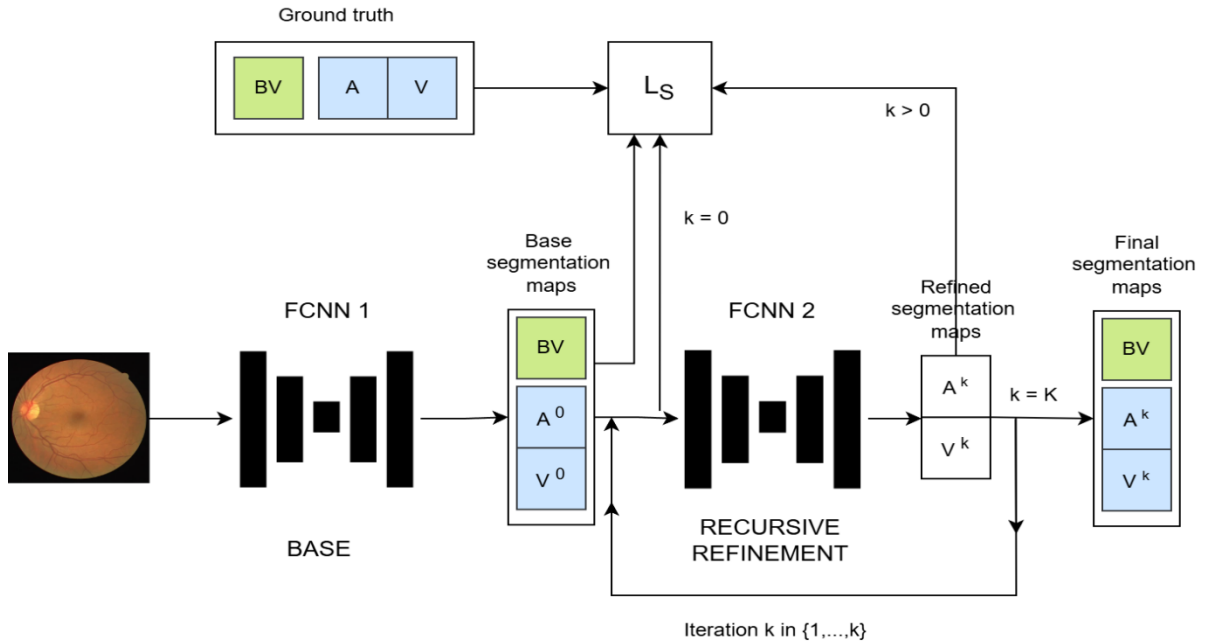


Fig 6.1 Architecture of RRWnet model

$k$ : Refinement iteration index (1 to  $K$ ) ,  $K$ : Total refinement iterations ,  $A^0, V^0$ : Initial artery and vein segmentation maps ,  $BV^0$ : Initial blood vessel (artery + vein) segmentation map ,  $A^k, V^k$ : Refined artery and vein maps at iteration  $k$  ,  $FCNN_1$ : Base network for initial segmentation |  $FCNN_2$ : Recursive refinement network ,  $L_s$ : Segmentation loss function.

### Advantages of RRWNet in AV Classification

One of the key benefits of RRWNet is its capacity to make several iterations of refinement, enhancing artery-vein separation without sacrificing the structural coherence of the vascular tree. The outcome of our experiments also offers proof that the Recursive Refinement (RR) subnetwork can serve as an independent post-processing module, supplementing the segmentation result provided by other methods.

### Comparison with U-Net-Based Models

In initial deployments, a standard U-Net architecture was employed for artery and veins data classification. The U-Net model, initially introduced by Ronneberger et al. [53], has become extremely popular in medical image segmentation due to its encoder-decoder structure with skip connections that allow precise feature localization. Later developments, e.g., U-Net++ [54], AV-Net, and Attention U-Net [55], improved feature fusion and segmentation performance by incorporating dense skip connections and attention mechanisms.

To enhance segmentation quality and overcome the limitations attained, we utilized RRWNet, which performed significantly better than the U-Net model. The results confirm the effectiveness of recursive refinement in enhancing AV segmentation and classification. The significant performance gains demonstrate RRWNet's ability to accurately define vascular structures, maintain topological consistency, and enhance classification accuracy over conventional FCNN-based approaches.

Utilization of RRWNet for artery-vein classification proved higher segmentation accuracy and vessel classification consistency than traditional U-Net –based approaches. Through iterative recursive refinement of the raw segmentation results, RRWNet successfully removes misclassification errors, thus producing more accurate and clinically relevant artery-vein classification. Moreover, the adaptability of the RR subnetwork as a post-processing module renders it more suitable for medical image analysis tasks.

## 6.4 RESULTS

The initial model employed for AV classification was U-Net, and its performance was tested against significant metrics such as Sensitivity, Specificity, and Accuracy. The output is low (as indicated in Fig 6.1) and is used as the baseline for comparison with improved models.

Table 6.1 U-Net base model results

METRIC	U-net
Sensitivity	62.5
Specificity	74.3
Accuracy	72.0

To further enhance AV classification, RRWNet, which shows progressive improvements over multiple training iterations. As shown in Figure 6.4, metrics such as Sensitivity, Specificity, and Accuracy consistently improved with each k –iterations. The result is shown in Fig 6.5

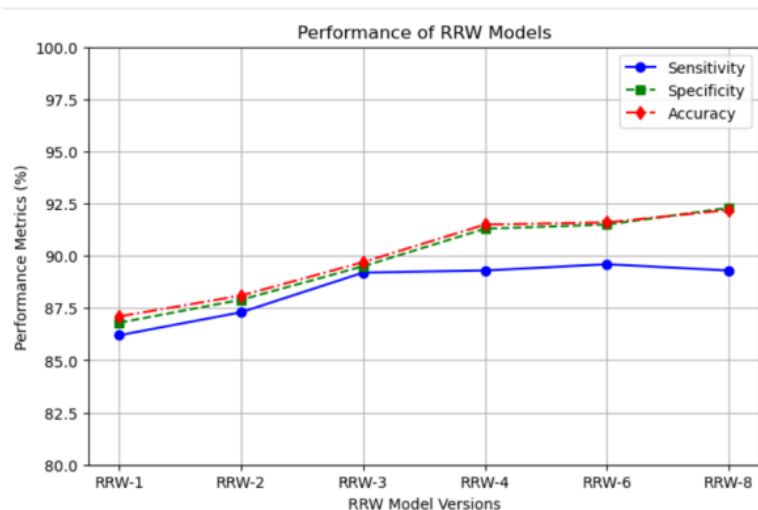


Fig 6.2 of RRWnet model version results



Fig 6.3 RRWnet output

The model was tested on the RITE dataset containing 40 images and the LES-AV dataset containing 22 images. Both datasets contain proper labels for AV classification. Upon testing, RRWNet achieved an accuracy of 83% on RITE and 86% on LES-AV. This indicates that it performs well with various datasets.

## CHAPTER 7

### ARTERIOVENOUS RATIO CALCULATION

#### 7.1 INTRODUCTION

After the successful segmentation of arteriovenous (AV) structures, the correct identification of vessel diameters is a vital next step in the study of retinal vasculature. This process helps to derive the Arteriovenous Ratio (AVR), a vital biomarker for evaluating the risk of cardiovascular disease (CVD). The vessel diameter measurement process consists of extracting vascular edges, defining centerlines, and computing diameters along the segmented vessels.

The main reasons for problems in measuring vessel diameter are changes in illumination, noise, and retinal vessel width. These challenges are addressed using a multi-step approach comprising centerline extraction, intensity-based edge detection, interpolation, and outlier filtering. Provided a comprehensive explanation of the vessel diameter calculation method, underlying mathematical formulas, and performance assessments.

#### 7.2 METHODOLOGY

To assess the Arteriovenous Ratio (AVR) for cardiovascular disease (CVD) detection, the follow up of a structured approach includes :

##### 7.2.1 Vessel Centerline Extraction

Once the vessels are segmented, the centerlines of each vessel must be accurately identified as a reference for measuring vessel diameters.

##### 7.2.1.1 Skeletonization

Skeletonization preserves the topology of the vessel structure while reducing it to a representation that is only one pixel wide. The centerline is extracted from the segmented vessel map using the Zhang-Seun thinning algorithm. This algorithm was selected because it effectively reduces width variability while maintaining vessel topology, which makes it appropriate for vascular segmentation.

The centerline extraction process can be represented mathematically as equation 7.1 :

$$S(V) = \lim_{n \rightarrow \infty} (V_n) \quad (7.1)$$

Where,

- $S(V)$  is the skeletonized vessel structure.
- $V_n$  represents the iterative thinning operation applied to the segmented vessel image  $V$ .

### 7.2.1.2 Bifurcation Removal

When estimating diameter, bifurcation points add uncertainty. Bifurcation points are found and eliminated using morphological operations and pattern recognition techniques. These techniques were chosen because they effectively improved measurement accuracy and decreased segmentation artifacts.

Mathematically, the bifurcation points  $Bp$  in a vessel image  $V$  can be detected using eq 7.2:

$$Bp = \{p \in V \mid N(p) > T\} \quad (7.2)$$

where,

- $N(p)$  is the number of neighboring pixels at point  $p$ .
- $T$  is the bifurcation threshold (typically  $T \geq 3$ )

.

### 7.2.1.3 Smoothing and Refinement

Gaussian filtering is used to refine the centerline and eliminate small discontinuities. While preserving vessel topology, ragged centerline points are smoothed by cubic spline interpolation. In image processing, the Gaussian filter is frequently used to reduce noise, and cubic spline interpolation guarantees a continuous and precise centerline representation.

The Gaussian smoothing operation is given by:

$$G(x) = \frac{1}{\sqrt{2\pi}\sigma} e^{-\frac{x^2}{2\sigma^2}} \quad (7.3)$$

where,

- $G(x)$  is the Gaussian function.
- $\sigma$  is the standard deviation of the Gaussian kernel.

## 7.2.2 Edge Detection for Diameter Measurement



To accurately measure the diameter, vessel edges must be detected along the normal directions to the centerline.

### 7.2.2.1 Normal Line Computation

At each point along the centerline, a normal line is computed. The orientation of the normal line is determined by estimating the local tangent direction using a **five-pixel neighborhood gradient approximation** to ensure robustness against noise [37].

The tangent direction at point  $p$  is computed as equation 7.4:

$$\theta_p = \tan^{-1}(\partial y \partial I \div \partial x \partial I) \quad (7.4)$$

where,

- $\partial x \partial I$  and  $\partial y \partial I$  are the image intensity gradients along the  $x$  and  $y$  directions.

The normal line at each centerline point  $p$  is given by equation 7.5:

$$N_p = (-\sin(\theta_p), \cos(\theta_p)) \quad (7.5)$$

### 7.2.2.2 Intensity Profiling

The vessel cross-section along each normal line is analyzed by extracting pixel intensity values. Vessels typically appear as low-intensity (dark) regions against a brighter background. The first-order derivative of the intensity profile helps identify significant transitions, marking the vessel boundaries [32]

Edge detection is performed using (equation 7.6):

$$E(x) = dI/dx \quad E(x) = \frac{dI}{dx} \quad E(x) = dx dI \quad (7.6)$$

where,

- $E(x)$  is the edge response.
- $I(x)$  is the intensity function along the normal line.

### 7.2.2.3 Clustering-Based Edge Detection

A k-means clustering algorithm is applied to the intensity profile [33]. Pixels are classified into three groups: vessel interior, vessel edge, and background. The transition points between vessel interior and background define the vessel boundaries.

Mathematically, k-means clustering aims to minimize using equation 7.7:

$$J = \sum_{i=1}^k \sum_{j=1}^n \|x_j - c_i\|^2 \quad (7.7)$$

where,

- $k$  is the number of clusters.
- $x_j$  is the pixel intensity value.
- $c_i$  is the cluster center.

### 7.2.3 Vessel Diameter Computation

To assess the vessel diameter computation, we follow a structured approach which includes :

#### 7.2.3.1 Interpolation-Based Smoothing

Noise and variations in intensity introduce errors; therefore, a moving average filter is applied to smooth diameter measurements while preserving vessel structures

The moving average filter is defined as:

$$Ds(i) = \frac{1}{N} \sum_{j=i-N}^{i+N} D(j) \quad (7.8)$$

where,

- $Ds(i)$  is the smoothed diameter at index  $i$ .
- $N$  is the window size.
- $D(j)$  is the raw diameter measurement.

#### 7.2.3.2 Outlier Removal

Statistical outlier detection is applied where values deviating beyond two standard deviations from the local mean are excluded to improve accuracy [35]

Outliers are identified using:

$$D(i) \in [\mu - 2\sigma, \mu + 2\sigma] \quad (7.9)$$

where,

- $\mu$  is the mean diameter.
- $\sigma$  is the standard deviation.

### 7.2.3.3 Weighted Averaging for AVR Calculation

Vessel diameters within a predetermined Region of Interest (ROI) are subjected to weighted averaging in order to guarantee reliable AVR computation. Vessel clarity and segmentation confidence levels are used to determine the weighting factors [36]. By giving high-confidence measurements priority, this method increases the accuracy of AVR computations.

To ensure robust AVR computation, weighted averaging is applied to vessel diameters within a predefined **Region of Interest (ROI)**.

$$D_w = \sum i = 1 n w_i \sum i = 1 n w_i D_i \quad (7.10)$$

where,

- $D_w$  is the weighted diameter.
- $W_i$  is the confidence weight.

### 7.2.4 Arteriovenous Ratio (AVR) Calculation

The AVR is a widely used clinical metric for assessing cardiovascular health by comparing the relative widths of arterioles and venules in the retina , It is calculated as:

$$AVR = \frac{D(a)}{D(v)} \quad (7.11)$$

where,

- $D(a)$  = average diameter of selected arterioles.
- $D(v)$  = average diameter of selected venules.

#### 7.2.4.1 Selection of Vessel Segments

AVR is calculated within a specific retinal region, typically 0.5 to 1.0 disc diameters from the optic nerve head (Zone B) to ensure consistency [27]. This standard is widely used in ophthalmology studies to improve reproducibility.

### 7.2.4.3 Diameter Normalization

Vessel diameters are normalized using a reference scale to account for variations in image resolution and patient-specific anatomical differences [33]. This ensures accurate cross-study comparisons.

### 7.2.4.4 AVR Thresholds for Cardiovascular Risk Assessment

- Normal AVR: 0.67 - 0.75.
- Mild Narrowing: 0.55 - 0.66 (moderate vascular risk).
- Severe Narrowing: < 0.55 (high cardiovascular risk) [29].

These threshold values are based on well-established clinical studies linking AVR to cardiovascular disease risk.

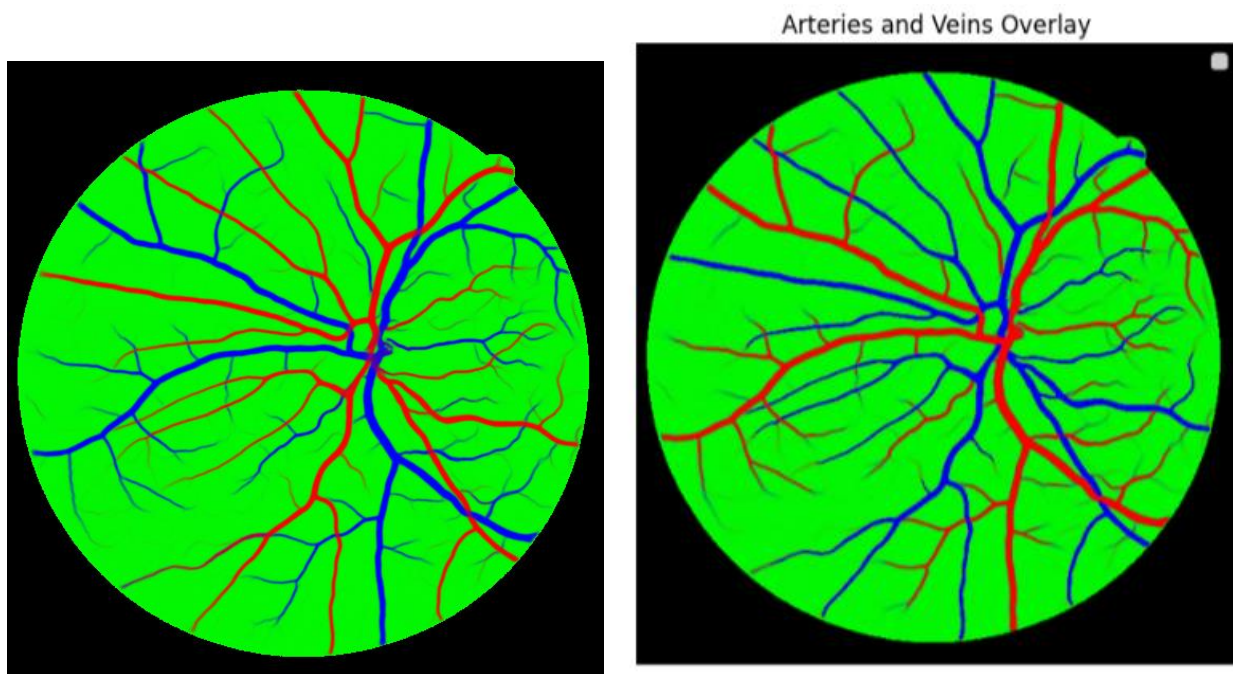
## 7.3 AVR – Results:

Table 7.1 The vessel diameter measurement results

Image Name	Avg. Artery Diameter	Avg. Vein Diameter	AV Ratio (AVR)	Risk Assessment
01_test	10.68 in pixels	19.53 in pixels	0.547	Low
04_test	13.41 in pixels	18.71 in pixels	0.717	Normal
07_test	13.36 in pixels	22.54 in pixels	0.593	Low
10_test	11.91 in pixels	21.32 in pixels	0.559	Low
16_test	14.83 in pixels	18.44 in pixels	0.804	Normal
19_test	11.07 in pixels	20.71 in pixels	0.535	High

To support the vessel diameter measurements, Figure 7.1 illustrates key processing stages including vessel segmentation, classification into arteries and veins, and application of distance transforms to determine vessel calibers. These steps are fundamental for accurate AV ratio computation.

Visualization of AV ratio analysis pipeline.



*Fig 7.1* Arteries and veins overlay (red and blue, respectively).

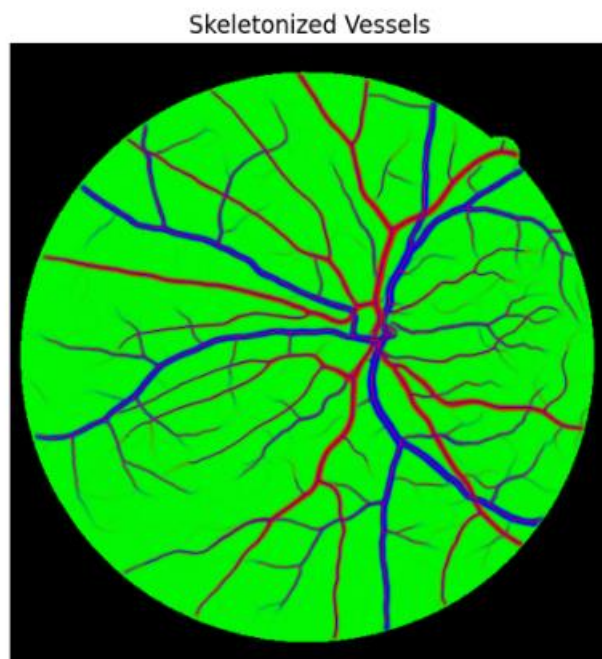


*Fig 7.2:* Skeletonized vessel structures

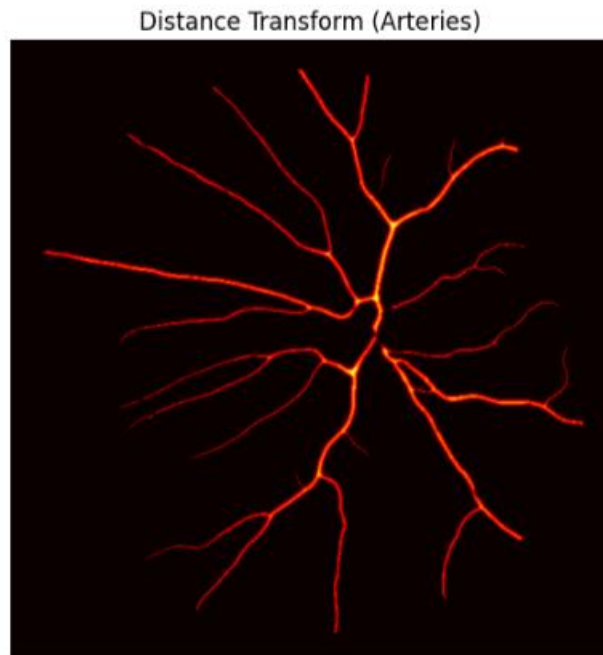


*Fig 7.3:* Distance transform on artery segments.

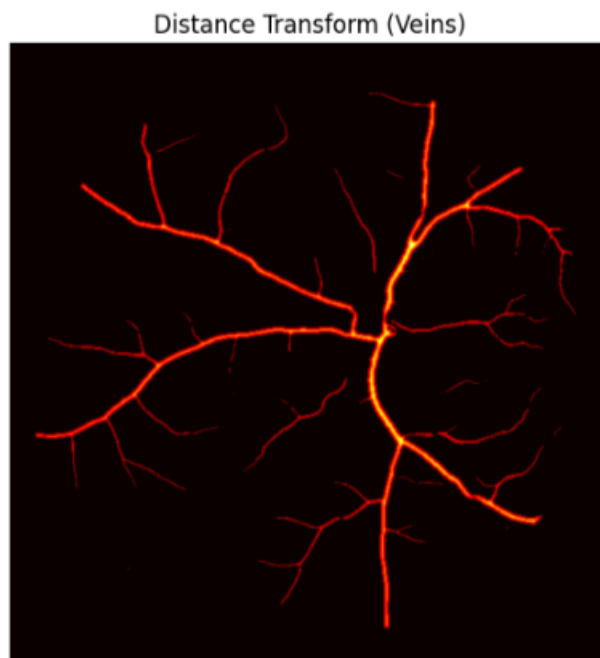


*Fig 7.4:* Distance transform on vein segments.

Four important steps in the AV ratio calculation process are depicted in the figure. In order to clearly distinguish between different types of vessels, Fig 7.1 overlays segmented arteries (in red) and veins (in blue) on the original retinal image. These vessels are skeletonized in the Fig 7.2 , which reduces them to their centerlines for accurate structural analysis. The distance transform is applied to arteries and veins in the Fig 7.3 and Fig 7.4, respectively, emphasizing vessel thickness and facilitating precise diameter measurements that are essential for calculating the AV ratio.

Table 7.2 . Performance Metrics of AVR Computation

Metric	Value
Mean Absolute Error (MAE)	2.2041
Standard Deviation (SD)	4.5173
Correlation Coefficient (R <sup>2</sup> )	0.7124

With an AVR value of 0.7171, the results displayed in Table 7.1 clearly distinguish between the average arteriole and venule diameters. This value, which is within the normal physiological range ( $\geq 0.67$ ), shows that the vascular structure is healthy and free of abnormalities or significant narrowing. The absence of early-stage cardiovascular problems in the retinal image under examination is further supported by the classification based on this AVR value, which is "Normal AVR – Low Risk." The AVR computation pipeline's performance evaluation metrics are shown in Table 7.2. The artery and vein diameter profiles show good agreement and acceptable measurement consistency with a correlation coefficient (R<sup>2</sup>) of 0.7124, a mean absolute error (MAE) of 2.2041, and a standard deviation (SD) of 4.5173. These results validate the robustness and reliability of the AVR assessment methodology in clinical retinal image analysis.

The performance measures listed in Table 7.2 show that the AVR calculation model reflects fairly decent predictive power. The Mean Absolute Error (MAE) of 2.2041 that is obtained implies that the average of the forecasted AVR values will differ from the actual values by approximately 2.2 units, which is a moderate degree of accuracy. Standard Deviation (SD) of 4.5173 means there is some uncertainty in the error in prediction, suggesting that while most of the predictions are similar to the true values, a few may deviate substantially. The value of the Correlation Coefficient (R<sup>2</sup>) of 0.7124 indicates that the predicted and actual AVR values show strong positive correlation, which indicates that the model accounts for roughly 71% of the variability in the data. Overall, these statistics indicate that the AVR calculation model is dependable, although there remains potential for improvement in decreasing variability and improving accuracy.

## **CHAPTER 8**

### **OPTIC CUP DISK SEGMENTATION AND OPTIC CUP-DISK RATIO CALCULATION**

#### **8.1 INTRODUCTION**

Automated optic cup and disc segmentation is essential for retinal image analysis in the context of cardiovascular disease (CVD) screening. Based on our survey of the literature I have chosen a YOLO-based approach, namely an improved YOLOv8 model, has been carefully crafted to detect and outline these important anatomical structures accurately. Optic cup and disc segmentation is critical in the computation of the Cup-to-Disk Ratio (CDR), a crucial biomarker whose ratio of more than 0.6 is clinically important, reflecting a higher risk of CVD. To obtain effective and accurate segmentation, the system uses a custom-developed preprocessing algorithm called YR-Adapter, which effectively derives boundary coordinates from grayscale retinal images. In addition, the model utilizes a state-of-the-art loss function—Focal Enhanced Intersection over Union (Focal-EIoU) loss—rather than the traditional CIoU loss. The new loss function incorporates a focal weighting mechanism to focus on hard examples with small overlaps and solves problems with center distance and aspect ratio difference, thus improving both training convergence speed and final segmentation accuracy.

#### **8.2 ALGORITHM FOR CALCULATING CUP DISK RATIO**

- Preprocessing & Boundary Extraction (YR-Adapter):
  - Convert retinal images to grayscale and normalize intensities.
  - Traverse each row to identify and extract the leftmost and rightmost boundary points of the optic cup and disc.
  - Sort the boundary points clockwise to form continuous contours.
- YOLOv8-Based Segmentation:
  - Adapt the YOLOv8 segmentation model to output detailed segmentation maps.
- Loss Function Optimization:
  - Replace the conventional CIoU loss with the Focal-EIoU loss to focus on challenging examples by applying a focal weighting mechanism.
  - Penalize errors in overlap, center distance, and aspect ratio more effectively.
- Cup-to-Disk Ratio (CDR) Calculation:
  - Compute the segmented areas of the optic cup and disc.
  - Calculate CDR by finding the ratio of segmented areas of optic cup and disc, with a value  $> 0.6$  indicating potential CVD risk.



### 8.3 METHODOLOGY FOR CALCULATING CUP DISC RATIO

The process involves a number of well-coordinated steps, starting with dataset preparation and annotation, then preprocessing, training the model, and optimization, and finally the automated calculation of the CDR. Specialist annotators use software like CVAT(Computer Vision Annotation Tool)(In Fig 8.1) to create accurate polygon-based annotations for the optic disc and cup, making sure that the ground truth is accurate and detailed.

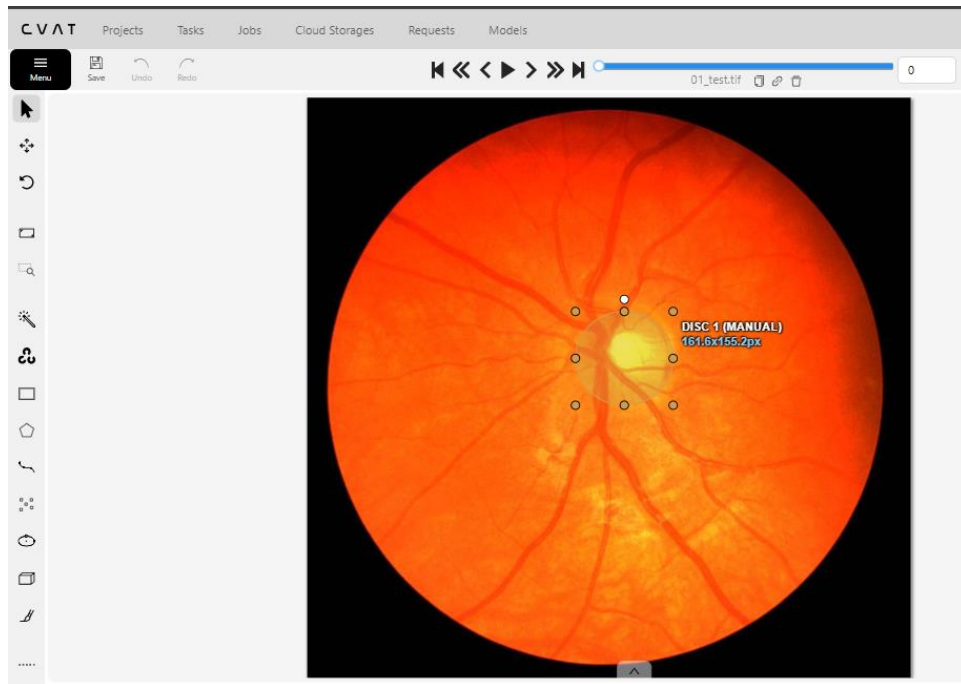


Fig 8.1 Annotation of cup and disc Using CVAT for retinal images

This is followed by all retinal images entering a preprocessing step during which they are normalized and converted into grayscale. YR-Adapter algorithm is then in the background, scanning every row of an image very carefully to pull out the accurate boundary locations of the optic structures and then normalizing it. This is a step of finding and categorizing left and right most pixels in a clockwise direction, which is crucial for generating continuous contours to be used as the basis for training the segmentation model. The illustration below describes how the binary masks is being transformed into yolo acceptable input which can be utilized for training.

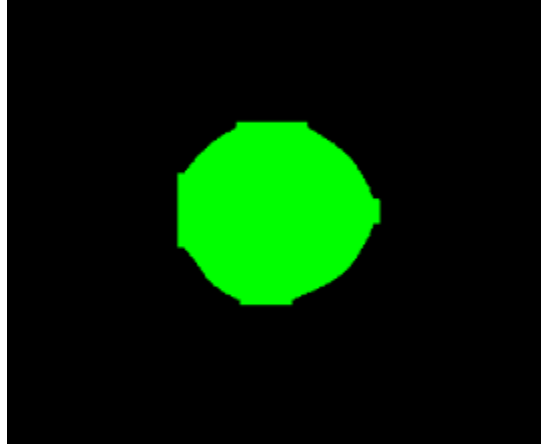


Fig.8.2. Annotated mask of segmented retinal image

Here u can see that the annotated mask (Fig 8.2) is being converted to the YOLOv8 acceptable input format (Fig 8.3) using the YR-Adapter.

```
01_train.txt - Notepad
File Edit Format View Help
0 0.506507 0.368750 0.498498
0.474474 0.376042 0.469469
0.445445 0.391667 0.440440
0.421421 0.416667 0.419419
0.405405 0.456250 0.404404
0.410410 0.506250 0.414414
0.433433 0.541667 0.440440
0.464464 0.563542 0.469469
0.492492 0.572917 0.498498
```

Fig.8.3 YR-Adapter Output

After extracting the boundaries, the trained enhanced YOLOv8 model is run on the preprocessed images. The model's architecture is customized to generate in-depth segmentation maps that retain the general global information and subtle local patterns required to properly define the optic cup and disc. During the training phase, hyperparameter tuning is carried out extensively, modifying parameters like the learning rate, batch size, and data augmentation strategies to ensure optimal performance. One key alteration in this regard is substituting the baseline Complete Intersection Over Union (CIoU) Loss with Focal-EIoU Loss, as presented in Equations (8.1) and (8.2).

Complete Intersection Over Union Loss(CIoU):

$$CIoU = 1 - IoU + \frac{d^2}{c^2} + \alpha * v \quad (8.1)$$

Where

- $d^2$ : Squared Euclidean distance between the box centers.
- $c^2$ : Diagonal length of the smallest enclosing box.
- $v$ : Diagonal length of the smallest enclosing box.
- $\alpha$ : A weighting factor.

Focal Enhanced Intersection Over Union Loss(Focal-EIoU):

$$\text{Focal - EloU} = (IoU)^2 * (1 - IoU + \text{Distance Loss} + \text{Aspect Ratio Loss}) \quad (8.2)$$

Where,

- $IoU^\gamma$ : Intersection over Union, with a focal term that emphasizes harder examples (typically  $> 1$ ).
- Distance Loss: It penalizes the center distance between predicted and ground truth boxes.
- Aspect Ratio Loss: It penalizes aspect ratio inconsistencies..

Through the inclusion of the focal weighting mechanism, the model is optimized to learn from hard examples to best reduce segmentation errors caused by small overlaps and unnatural aspect ratios. After training is finished, the model is then capable of generating highly precise segmentation results which can be further applied for further clinical analysis.

The final step in the methodology involves the calculation of the Cup-to-Disc Ratio (CDR). This is done by initially determining the areas of the segmented optic cup (SOC) and optic disc (SOD) using pixel counting. The last step in the methodology is calculating the Cup-to-Disc Ratio (CDR), as presented in Equation (8.3):

$$CDR = \frac{SOC}{SOD} \quad (8.3)$$

Where,

- $SOC$  is the area of the segmented optic cup.
- $SOD$  is the area of the segmented optic disc.

with a result greater than 0.6 being a risk indicator for potential CVD. This computer calculation not only facilitates the screening procedure but also allows clinicians to possess a strong quantitative measure that they can utilize in early diagnosis and intervention.

## 8.4 RESULT ANALYSIS

Table 8.1 YOLOv8 results

Model	Precision	Recall	F1 Score
<b>YOLO</b>			
Optic Cup	0.8012	0.8393	0.8150
Optic Disc	0.8950	0.8948	0.8949
<b>YOLO+FOCALELOU</b>			
Optic Cup	0.9013	0.8693	0.8850
Optic Disc	0.9972	0.9900	0.9936

From Table 8.1 the improved segmentation accuracy has a direct and significant effect on the calculation of the Cup-to-Disc Ratio, since more accurate delineation of the optic cup and disc results in a more accurate ratio. With the clinical significance of the CDR, which is a major indicator for CVD risk, the better performance of the model means a stronger and more reliable automated screening tool. The detailed assessment verifies that the YOLOv8 based solution, supported with sophisticated preprocessing and an optimized loss function, is a dramatic breakthrough in retinal image segmentation technology, with transparent advantages for cardiovascular disease early detection and intervention.

## **CHAPTER 9**

### **OPHTHALMIC BIOMARKERS ANALYSIS**

#### **9.1 INTRODUCTION**

Ophthalmic CVD Indicator is presented as a new parameter based on retinal image classification in order to incorporate cardiovascular disease (CVD) risk prediction using ophthalmic biomarkers. For generating feature maps, STARE dataset is used, containing retinal fundus images labeled over thirteen classes such as Normal(N), Coat Disease(CD), Macro aneurism(MA), Drusen(D), Background Diabetic Retinopathy(BDR), Proliferative Diabetic Retinopathy(PDR), Choroidal Neovascularization(CNV), Arteriosclerotic Retinopathy(AR), Hypertensive Retinopathy(HTR), Central Retinal Vein Occlusion(CRVO), Branch Retinal Vein Occlusion(BRVO), Hemi-Central Retinal Vein Occlusion(HCRVO), and Central/Branch Retinal Artery Occlusion(RAO). From the literature review we have found a list of ophthalmic abnormalities that may potentially be significant predictors of the development of cardiovascular risk factors. This feature map that we have derived can now be used to enhance the final data.

#### **9.2 RETINAL BIOMARKERS AND THEIR LINK TO CVD**

The presence of specific ophthalmic biomarkers in retinal images may signal underlying cardiovascular conditions. Retinal diseases like Background Diabetic Retinopathy (BDR), Proliferative Diabetic Retinopathy (PDR), Choroidal Neovascularization (CNV), Arteriosclerotic Retinopathy (AR), Hypertensive Retinopathy (HTR), and various forms of Retinal Vein Occlusion (CRVO, BRVO, HCRVO, RAO, etc.) are linked to CVD risk.

These biomarkers provide critical insights:

- Hypertensive Retinopathy (HTR) and Arteriosclerotic Retinopathy (AR) suggest long-term vascular stress and hypertension, both strong predictors of CVD.
- Diabetic Retinopathy (BDR, PDR) reflects microvascular damage, which often coexists with cardiovascular complications.
- Choroidal Neovascularization (CNV) is linked to systemic vascular abnormalities, increasing the likelihood of cardiovascular risks.
- Retinal Vein Occlusions (CRVO, BRVO, HCRVO, RAO, BRAO) indicate thrombotic events and poor blood flow, which correlate with stroke and heart disease.

#### **9.3 CORRELATION ANALYSIS OF RETINAL BIOMARKERS AND CVD**

## Introduction To Correlation

Correlation is a statistical measure quantifying the extent to which two variables vary together. It reflects both the strength and the direction. Practically speaking, when one variable rises and the other tends to rise as well, the phenomenon is referred to as positive correlation; if one variable rises and another falls, then the phenomenon is referred to as a negative correlation. Correlation does not cause causation, but it tells us a lot about how the variables are related to each other, which is useful for prediction purposes and getting insight into hidden patterns in the data. There are very few sections below talking about the different ways of correlating the variables.

## Pearson Correlation Coefficient

The Pearson correlation coefficient is most commonly used test to measure the strength of a linear relationship between two continuous variables. It will give a figure ranging from  $-1$  to  $+1$ , of which  $-1$  would represent an exact negative linear relationship, and  $+1$  will represent an exact positive linear relationship, while  $0$  will reflect no linear relationship whatsoever. This coefficient requires the two variables to be normally distributed, linearly related, and have homogeneity of variance. Notably, in the case of binary data (coded as  $0$  and  $1$ ), the Pearson correlation coefficient is equal to the phi coefficient. This correspondence renders it especially well-suited for situations where the two variables are binary, like in our situation where retinal biomarkers and CVD risk are evaluated as absent or present. The calculation of the Pearson correlation coefficient involves Equation (9.1), which measures the linear relationship

**Formula:**

$$r = \frac{\sum (x_i - x_{mean})(y_i - y_{mean})}{\sqrt{\sum (x_i - x_{mean})^2} \sqrt{\sum (y_i - y_{mean})^2}} \quad (9.1)$$

Where,

- $x_i, y_i$  are the values of variables  $x$  and  $y$ .
- $x_{mean}, y_{mean}$  are the mean values of  $x$  and  $y$ .

## Spearman's Rank Correlation Coefficient:

Spearman's rank correlation coefficient quantifies the strength and direction of a monotonic relationship between two variables by ranking the data. This technique is perfect when the data are ordinal or where the normality assumptions necessary for Pearson's correlation are violated. But when used on binary data, the ranking procedure provides no additional insight since there are just two different values, and the results are essentially the same as those from the Pearson correlation. In contrast to Pearson's correlation, which presumes linearity, Spearman's correlation will still function if the relationship is non-linear but monotonic (i.e., always increasing or

always decreasing). Although Spearman's approach is strong for non-linear monotonic relationships, it is less useful when the data is binary. Therefore, Spearman's correlation is not needed in our scenario. As indicated in Equation (9.2), Spearman's rank correlation takes ranking differences into account.

**Formula:**

$$\rho = 1 - \frac{6 \sum d_i^2}{n(n^2-1)} \quad (9.2)$$

Where,

- $d_i$  is the difference between the ranks of each pair of observation.
- $n$  is the total number of observations.

**Kendall's Tau Coefficient**

Kendall's tau coefficient is another non-parametric estimate that measures the relationship between two variables by comparing concordance and discordance of paired observations. It comes in handy under conditions of small sample sizes or when there are many tied ranks in the dataset. Similar to Spearman's rho, Kendall's tau gives a scale that varies from  $-1$  to  $+1$ , and values tending towards these extremes show strong associations. However, with respect to binary data, with none distinct ranks, Kendall's tau does not provide extra advantages compared to the Pearson correlation. Having binary values simply results in outcomes that reflect the same as from the Pearson method, thus making it a less useful option when comparing binary-to-binary. Kendall's tau is normally applied to ordinal or ranked data, which is not the case with our data set. Equation (9.3) represents Kendall's tau, which is applied in rank-based correlation analysis.

**Formula:**

$$\tau = \frac{C - D}{C + D} \quad (9.3)$$

Where,

- $C$  is the number of concordant pairs (where both variables increase or decrease together)
- $D$  is the number of discordant pairs (where one variable increases while the other decreases)

**Point-Biserial Correlation**

The point-biserial correlation is particularly calibrated to quantify the association between a single continuous variable and a single binary (dichotomous) variable. It is algebraically

identical to the Pearson correlation if one variable is binary. Nevertheless, in our application—where the retinal biomarkers and CVD risk are both binary—the point-biserial correlation cannot be used. Because neither variable is continuous, it would not be suitable to use a technique designed for binary-continuous pairs. Thus, point-biserial method is not included in our consideration in place of methods that truly represent the binary nature of both variables. As demonstrated by Equation (9.5), below is the formula for Point-Biserial partial correlation.

**Formula:**

$$r_{pb} = \frac{\bar{x}_1 - \bar{x}_0}{\bar{a}} \times \sqrt{\frac{n_1 n_0}{(n_1 + n_0)^2}} \quad (9.4)$$

**Where,**

- $\bar{x}_1, \bar{x}_0$  is the mean of continuous variable for groups **1** and **0**.
- $s$  is the standard deviation of continuous variable.
- $n_1, n_0$  is the sample sample sizes for groups **1** and **0**.

### **Applicability to Our Use Case**

In our data, both the retinal biomarkers and CVD risk are binary variables, so each is merely "present" or "not present." This renders the Pearson correlation coefficient the most suitable measure since, when used with binary data, it effectively works as the phi coefficient—a long-standing measure of association between two binary (dichotomous) variables ranging from -1 to +1, measuring the strength and direction of their relationship. Techniques such as Spearman's rank and Kendall's tau, although strong for ordinal or non-linear data, are of little benefit here because of the narrow range of binary variables. Similarly, point-biserial correlation is inappropriate since it's designed for the situation where one of the variables is continuous. According to our analysis the data has been computed using Pearson correlation coefficient. Fig 9.1 records Pearson correlation analysis findings between Cardiovascular risk and Ophthalmic biomarkers.



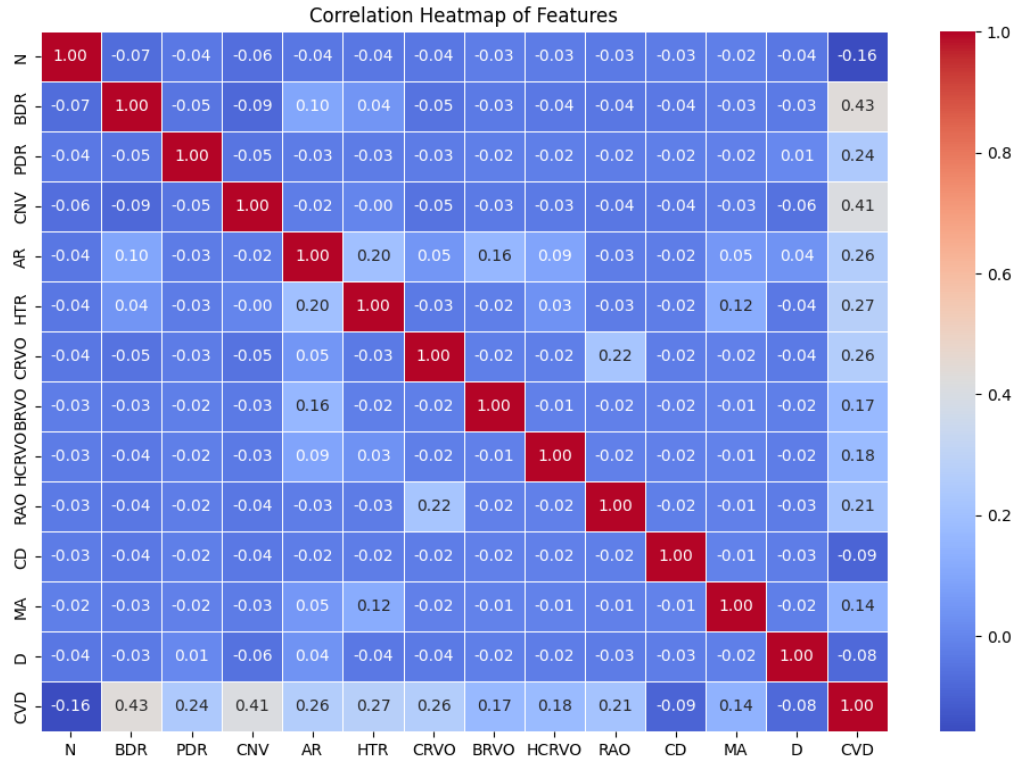


Fig 9.1 correlation heatmap of ophthalmic biomarkers and CVD

To quantify the relationship between ophthalmic biomarkers and CVD, a correlation heatmap was generated. The findings indicate:

- BDR (0.43), CNV (0.41), and PDR (0.24) show strong positive correlations with CVD, meaning these conditions are significant indicators of cardiovascular risk.
- HTR (0.27) and AR (0.26) also display moderate correlation, reinforcing the idea that vascular abnormalities in the retina align with systemic vascular disease.
- CRVO (0.17), BRVO (0.18), and HCRVO (0.21) have weaker but notable associations, suggesting that occlusive retinal diseases could still be risk factors for CVD.
- Normal (N) category has a negative correlation (-0.16), which confirms that healthy retinas are less likely to be associated with CVD.

## **CHAPTER 10**

### **FRACTAL DIMENSION**

#### **10.1 INTRODUCTION**

Fractal Dimension (FD) is an idea from mathematics to describe the self-similarity and complexity of natural structures. While Euclidean dimensions are whole numbers, FD is a non-integer value that tells us how detail in a pattern varies with scale. The human retinal vasculature is an example of a fractal structure, and is self-similar because its smaller portions provide a similar resemblance to the full structure. Measuring FD provides a measure of the density and complexity of branching in the vascular networks. Higher FD values show a more complex and well-distributed vascular pattern, whereas lower FD values indicate sparser vasculature and potentially disordered vasculature that may be diseased.

If the retinal vessels demonstrate complexity or branching that indicates their overall health, then they could also help predict carotid disease (CVD) following the advice of FD. The results of this study found that certain retinal signs such as arteriovenous nicking have inconsistent association with subclinical atherosclerosis and are not significantly associated with cardiovascular disease or stroke. Hence, relying only on AV ratio in some cases might not provide a complete cardiovascular risk assessment.

AV nicking demonstrates structural changes of a vessel. This is likely due to age or due to hypertension. It is a localized feature as it looks only at the artery vein widths, instead of the whole vessel. In cases where there is AV nicking (which may also be referred to as AV narrowing and the AV ratio might be 0.5 - 0.6, then FD can be evaluated as it indicates CVD. FD, again as stated has been shown to indicate branching and complexity of vessels. Even if the AV is lightly nicked it may still have a healthy FD a fact that could mean that the patient is still not safe for CVD.

#### **10.2 METHODOLOGY FOR FINDING FRACUAL DIMENSIONS**

##### **10.2.1 BOX COUNTING METHOD**

Among various methods for FD calculation, the box-counting method is widely used due to its simplicity and robustness in analyzing biological structures.

The box-counting method is a widely used technique for estimating the fractal dimension of irregular structures, particularly those that exhibit self-similarity, such as retinal vasculature. The method involves covering a binary image of the vascular structure with grids of assorted sizes and counting the number of occupied grid cells at each resolution.

The box counting method uses boxes whose sizes are based on powers of two to make sure that the image is analyzed at multiple scales, capturing its structural complexity. The calculation starts by extracting the height and width of the binary vessel image that was obtained by segmenting the

veins from the retinal image. The smallest dimension is chosen, and the half of the smaller dimension will determine the largest size box for counting solutions in the background to make sure the image was not subdivided into excessively large sections. For every box size, the algorithm reformats the image into sections of the size specified, and counts the number of boxes containing at least one pixel that was identified as a surface vessel pixel (Figure 10.2). The counts are recorded for each box size and turn into an estimating the fractal dimension using a log-log regression of the number of occupied boxes as a function of the inverse box size as suggested in 10.1. If calculated correctly, the slope from the log-log regression equals the fractal dimension giving a quantitative value to the complexity of the vessels network. A fractal dimension of greater than 1.3 indicates a close and complex branching pattern of a healthy microvascular networks and a lower fractal dimension of less than 1.3 indicative of vessel rarefaction that may be elevated due to complications such as diabetic retinopathy, hypertension etc.

The fractal dimension,  $D_f$  is given by

$$D_f = \lim_{e \rightarrow 0} \frac{\log(N(e))}{\log(\frac{1}{e})} \quad (10.1)$$

Where,

- $N(e)$  is the number of boxes of size  $e$  that contain part of the vascular structure.
- $e$  is the side length of the square grid.

### Algorithm for Box-Counting FD Calculation

#### Step 1: Image Preprocessing

- Retinal fundus images are obtained and converted into grayscale.
- Vessel segmentation is performed using edge detection or deep learning-based methods like U-Net.
- The image is binarized, with blood vessels appearing as white pixels on a black background.

#### Step 2: Grid Overlay and Box Counting

- A square grid of size  $e$  is superimposed on the image.
- The number of non-empty boxes (containing vessel pixels) is counted:  $N(e)$
- The grid size  $e$  is progressively reduced, and  $N(e)$  is recorded at each scale.

#### Step 3: Log-Log Plot and FD Estimation

- The values of  $\log(N(e))$  are plotted against  $\log(1/e)$
- The slope of the fitted line gives the fractal dimension  $D_f$
- 

### Limitations of the Box-Counting Method

While the box-counting approach is widely used, it has several limitations:

1. Dependence on Image Quality

- a. Retinal images may have noise, low contrast, or segmentation errors, affecting FD accuracy.
2. Loss of Structural Information
  - a. The method does not differentiate between arterioles and venules, which may have different implications for CVD risk (Cheeseman & Vrscaj).
3. Limited to 2D Projections
  - a. Retinal vasculature is a 3D structure, but box-counting is applied to 2D images, leading to information loss.
4. Overestimation in Sparse Networks
  - a. Sparse or disconnected vascular networks may result in artificially high FD values.
5. Lack of Standardization
  - a. Different grid sizes, segmentation techniques, and thresholding methods may produce inconsistent results across studies.

### 10.2.2 MINKOWSKI-BOULIGAND METHOD

To address these limitations, the Minkowski–Bouligand (MB) method, also known as the dilation method, is a refined approach that overcomes some limitations of traditional box-counting. The MB method calculates FD by dilating a structure with discs of varying radii and assessing how the area occupied by the structure changes

The Minkowski–Bouligand FD is derived by dilating a binary image of the retinal vasculature and measuring how the area occupied by the structure scales with the dilation size. Unlike box-counting, which overlays a grid, the MB method expands vessel structures using circular neighborhoods, making it more suitable for biological networks like the retinal vasculature.

The FD is calculated using:

$$Df = \lim_{\epsilon \rightarrow 0} \frac{\log(A(\epsilon))}{\log\left(\frac{1}{\epsilon}\right)} \quad (10.2)$$

Where,

- $A(\epsilon)$  is the area occupied by the dilated structure at scale  $\epsilon$
- $\epsilon$  is the dilation radius.

The segmented vessels are dilated using morphological structuring elements of increasing radii ( $\epsilon$ ), and for each dilation step, the area occupied by the dilated vessels ( $A(\epsilon)$ ) is measured. This is shown in 10.2. One way to get dilation is through Euclidean distance transform (EDT). Given a binary image, EDT generates an image where each pixel stores a value that corresponds to its distance from the nearest point of the object. This image is known as a distance map (DM). A log-log plot of  $A(\epsilon)$  versus  $\epsilon$  is generated, and the fractal dimension ( $D$ ) is computed as the slope of the linear region of this plot. A lower fractal dimension indicates a loss of vascular complexity, which has been associated with cardiovascular diseases, hypertension, and stroke

Higher FD values indicate denser, more complex vascular networks, while lower FD values suggest vascular rarefaction, a marker of microvascular disease.

## Algorithm for Minkowski–Bouligand FD Calculation

### Step 1: Image Preprocessing

- **Input:** Retinal fundus images.
- **Vessel Segmentation:** Extract vascular structures using

### Step 2: Morphological Dilation

- A circular structuring element of radius  $e$  is used to **dilate** vessel pixels.
- The **area** occupied by the dilated vessels  $A(e)$  is computed for various values of  $e$

### Step 3: Log-Log Plot and FD Estimation

- The values of  $\log(A(e))$  are plotted against  $\log(1/e)$  in Fig 10.1.
- The slope of the fitted line gives the **fractal dimension**  $D_f$

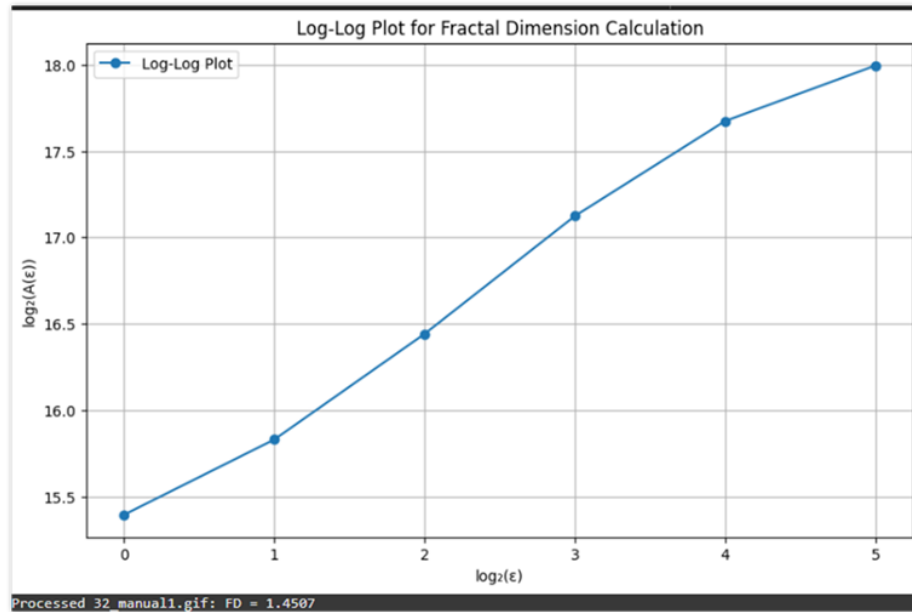


Fig 10.1: Log-Log plot for dilation method

Here,  $A(e) \propto e^{-D}$  where  $A(e)$  is the area covered by boxes and  $e$  is the box size.  $D$  is the estimated fractal dimension

Taking log on both sides:

$$\log(A(e)) = -D \log(e) + c \quad (10.3)$$

From this  $D$  is the negative slope of the log-log plot.

From [10.3],

$$FD = 2 - \lim(\log(A(e)))/(\log(e)) \quad (10.4)$$

So, in this instance assume two coordinates on the plot (18,5) and (16.4,2)

Finding the slope i.e.,

$$(\log(A(e)))/(\log(e)), \Rightarrow 0.55 \text{ approx.} \quad (10.5)$$

Substitute this value in (10.4) to get  $2 - 0.55$  which is  $FD = 1.45$  as achieved.

### 10.2.3 SANDBOX METHOD

The sandbox method is a technique used for calculating the fractal dimension of structures, particularly in analyzing complex patterns like biological structures, vascular networks, and other natural phenomena. It's especially valuable in medical imaging and biological systems analysis.

The sandbox method operates by measuring how a property (typically mass or pixel count) scales with increasing area or volume. Here's how it works:

#### 1. Basic Procedure:

- a. Randomly select points on the object or pattern as centers
- b. Create "sandboxes" (squares or circles in 2D, cubes or spheres in 3D) of increasing sizes around these centers
- c. Count the number of pixels or points of the pattern contained within each sandbox
- d. Plot the logarithm of the count versus the logarithm of the sandbox size
- e. Calculate the slope of this log-log plot, which gives the fractal dimension

2. **Mathematical Representation:** If  $N(r)$  represents the number of pixels within a sandbox of radius  $e$ , then:  $N(e) \propto e^D$  where  $D$  is the fractal dimension. Taking logarithms:  $\log(N(e)) = D \times \log(e) + c$ . The fractal dimension  $D$  is the slope of this relationship.

### FINAL COMPARISON

Below is a comparison of the methods used with their respective advantages, limitations, and approaches:

#### Box-Counting Method:

- Approach: Overlay a grid of boxes of varying sizes onto the structure and count the number of boxes that contain part of the structure.
- Fractal Dimension: Calculated based on how the number of occupied boxes scales with box size.
- Advantages: Simple implementation and widely used.
- Limitations: Sensitive to grid positioning and may suffer from edge effects.

### Minkowski–Bouligand (Dilation) Method:

- Approach: Dilate the structure by adding a buffer of a certain thickness and measure how the volume (or area) of the dilated structure scales with the buffer thickness.
- Fractal Dimension: Derived from the scaling relationship between the dilated volume and the buffer thickness.
- Advantages: Provides a more intuitive understanding of structure thickness.
- Limitations: Computationally intensive for complex structures.

### Sandbox Method:

- Approach: Place a sandbox of increasing radius around reference points within the structure and count the number of structure points within the sandbox.
- Fractal Dimension: Estimated from the scaling of the number of points with sandbox radius.
- Advantages: Reduces edge effects and provides localized information. MDPI
- Limitations: More computationally demanding due to multiple calculations around each reference point.

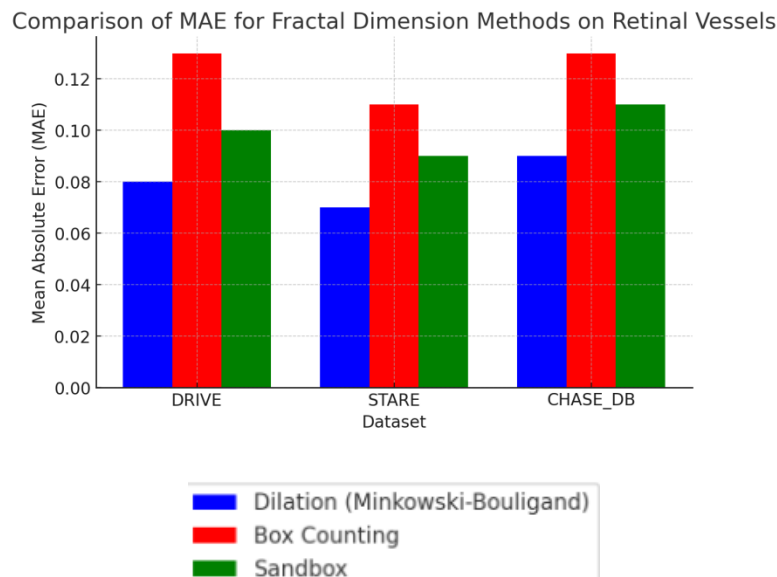


Fig 10.2: Comparison of methods

From the plotted Fig 10.2 it can clearly be inferred that there are several noises while using the box counting method thereby causing higher errors than the less noisy dilation method. For the chart, the mean MAE of all images in the three datasets were taken and plotted.

## 10.3 INFERENCE

## 1. FD as a Biomarker for CVD

Fractal Dimension (FD) of retinal vessels has emerged as a promising biomarker for cardiovascular diseases (CVD) due to its ability to quantify vascular complexity. Several studies have demonstrated that:

Lower FD is associated with higher risk of CVD, including stroke, hypertension, and coronary artery disease.

Higher FD is indicative of better vascular health and efficient blood flow regulation.

## 2. FD Calculation Methods and Their Impact

Various methods are used to estimate FD, and their accuracy influences clinical reliability:

**Minkowski–Bouligand (Dilation Method):** Most accurate with the lowest Mean Absolute Error (MAE). It provides a smoother and more precise FD estimation, making it preferable for CVD risk prediction.

**Sandbox Method:** Performs better than Box Counting but is still not as precise as the Minkowski–Bouligand approach.

**Box Counting Method:** Generally overestimates or underestimates FD due to sensitivity to noise and vessel segmentation errors, making it less reliable for clinical use.

## 3. FD and Vessel Density Correlation

A strong positive correlation exists between FD and vessel density, as seen in the DRIVE dataset. It can be observed in Fig 10.3 where there is a direct proportionality between FD and vessel density. This suggests that denser vessel networks correspond to higher FD values, reinforcing the link between vascular complexity and CVD risk assessment.

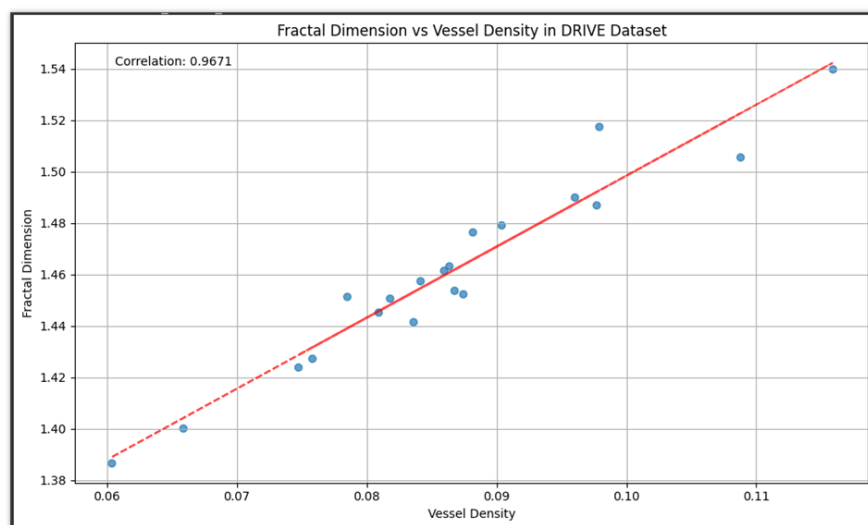


Fig 10.3: Vessel density-FD correlation



Looking at the relationship between fractal dimension and vessel density in this graph, several inferences can be made:

1. Physiological relationship: The strong positive correlation (0.9671) suggests that as blood vessels become more dense in the retina, they also form more complex branching patterns (higher fractal dimension). This likely reflects how vascular networks develop - as more vessels are needed to supply blood to tissues, they must create increasingly complex branching structures to efficiently cover the area.
2. Clinical implications:
  - a. This relationship could serve as a reference for normal vascular development
  - b. Deviations from this expected relationship might indicate pathology
  - c. For example, if a patient shows normal vessel density but abnormally low fractal dimension, it might suggest abnormal vessel development or remodeling
3. Diagnostic potential:
  - a. The predictable relationship means clinicians could potentially identify abnormal vasculature by measuring just one of these parameters
  - b. The relationship is so strong that outliers from this trend line could be flagged for further investigation
4. Methodological inference:
  - a. The linear nature of the relationship suggests these measures might be somewhat redundant in research - they capture related aspects of vascular structure
  - b. However, subtle differences in where specific samples fall relative to the trend line might reveal important biological variations
5. Quantitative model:
  - a. The precise linear relationship could be used to develop mathematical models of vascular development
  - b. This might help researchers understand how vessels grow and branch during development or disease progression

This graph essentially demonstrates that vessel complexity (fractal dimension) and vessel abundance (density) are intrinsically linked in what appears to be a fundamental biological relationship in vascular networks.

## CHAPTER 11

# Interpretability in Machine Learning Using Local Interpretable Model-agnostic Explanations (LIME)

## 1. Introduction

Interpretability of machine learning (ML) is the capacity to comprehend and explain the predictions of a model. Although models based on deep learning such as YOLO (You Only Look Once) have been very effective in applications such as vessel segmentation, they tend to be "black-box" systems. This lack of transparency is a major barrier to using them in high-risk fields such as healthcare, where professionals require access to the steps a model takes to arrive at its predictions. Therefore, individual predictions need to be explained to gain confidence in such models. On Implementation of LIME for YOLO model , which identifies Optic Cup and Disk in retinal image, gave better results than traditional Interpretability techniques i.e SHAP , GRAD-CAM , Anchors , Counterfactuals, Integrated Gradient and Random masking.

### 1.1 Objective

- **Analyzed and deployed LIME (Local Interpretable Model-agnostic Explanations)** as an explanation tool to interpret YOLO's vessel segmentation output in retinal images.
- **Compare LIME with other interpretability methods**, including:
  - SHAP (Shapley Additive Explanations)
  - Grad-CAM (Gradient-weighted Class Activation Mapping)
  - Integrated Gradients
  - Anchors
  - Counterfactuals
  - Random masking

- **Justified** why LIME is the most suitable approach for explaining YOLO's segmentation outputs in retinal imaging.
- **Improved transparency** in the model's decisions by making its predictions more interpretable.

## 2. Overview of LIME

### 2.1 What is LIME?

LIME is a model-agnostic explanation technique that is concerned with explaining an individual prediction of a machine learning model. It does this by generating locally faithful surrogate models that mimic the behavior of the black-box model locally around a given instance. LIME is desirable because it is able to explain model predictions in an interpretable, human-consumable way, which is necessary for applications such as medical imaging where model decisions must be explained to individuals without technical knowledge.

### 2.2 How LIME Works

LIME does this by generating altered instances close to the desired prediction of interest and subsequently training a simple surrogate model, e.g., linear regression, on these instances. The surrogate model is then used to estimate the opaque model's decision boundary close to the instance and thus provide an interpretable explanation of the prediction.

The LIME optimization process is governed by:

$$Loss(g) = Loss(f, g, \pi x) + \Omega(g) \quad (11.1)$$

In the Eq 11.1 ,

- $f$  is the black-box model,
- $g$  is the surrogate model,
- $\pi x$  is the proximity measure, and
- $\Omega(g)$  is a complexity penalty on the surrogate model

## **3. Types of Data LIME Can Be Applied To**

### **3.1 LIME for Tabular Data**

For tabular data, LIME perturbs individual features and creates synthetic samples to understand how small changes in the input affect the model's output. This perturbation is done while preserving the distribution of the data.

### **3.2 LIME for Text Data**

For text, LIME perturbs words or groups of words. By removing words and observing the model's output, LIME provides insights into the contributions of each word to the model's decision.

### **3.3 LIME for Image Data**

In order to process image data, LIME disturbs superpixels, which are collections of pixels with related characteristics. Superpixel-based perturbation enables the model to concentrate on regions that collectively influence the decision rather than individual pixels that might not have a major effect. Tasks like vessel segmentation in retinal images, where particular areas like veins and arteries matter, benefit greatly from this.

## **4. Advantages and Limitations of LIME**

### **4.1 Advantages of LIME**

- **Model-Agnostic:** Any machine learning model, including deep learning models like YOLO, can be used with LIME.
- **Local Interpretability:** LIME is more practical in real-world applications because it focuses on explaining individual predictions rather than trying to explain global behavior.
- **Human-Understandable Explanations:** Even non-experts can understand LIME's explanations because it relies on straightforward surrogate models, such as linear regression.
- **Efficiency:** Without requiring the original model to be retrained, LIME offers rapid insights.
- **Handles Non-Linearity:** LIME works well with complex models like CNNs (e.g., YOLO) because it locally approximates complex decision boundaries.

## 4.2 Limitations of LIME

- **Instability:** The explanations can vary between different runs due to the randomness in the perturbation process.
- **Local Approximation:** LIME only provides local explanations and cannot capture the global behavior of the model.
- **Computational Cost:** The process of generating perturbed samples can be slow for large datasets, requiring multiple iterations.
- **Superpixel Sensitivity:** For image data, LIME's effectiveness depends on the quality of the superpixel segmentation.

### LIME vs Other Interpretability Methods :

We are comparing LIME interpretability tool with Other interpretability tool for our YOLO model :

#### SHAP

Each prediction is given a feature importance score by SHAP (Shapley Additive Explanations). SHAP provides a global understanding of model behavior, in contrast to LIME, which is centered on local explanations.

- **Why LIME Is Better:** LIME offers more helpful local, interpretable explanations for comprehending particular predictions. SHAP may not be as useful for tasks where comprehending individual predictions is essential, even though it is useful for global analysis.

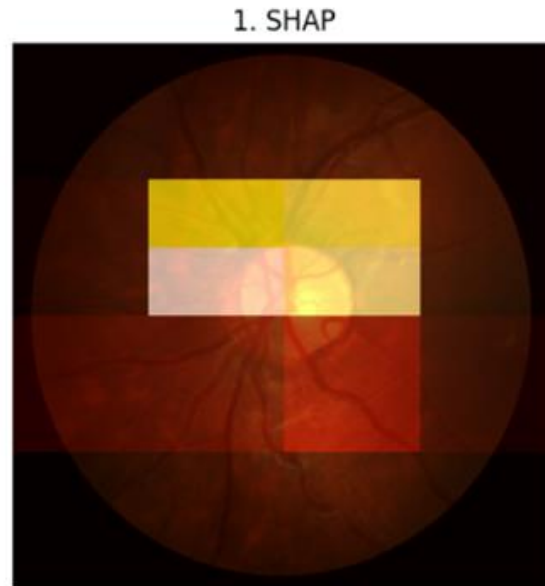


Fig 11.1 SHAP Results

- When comparing SHAP and LIME, we can observe that SHAP's explanations emphasize the importance of global features throughout the model. However, compared to LIME, the SHAP explanation for YOLO's vessel segmentation in Fig. 11.1 is less focused and fails to highlight particular areas of the image. The picture demonstrates how SHAP offers a general understanding but falls short of LIME's localized clarity.

### Grad-CAM

To determine which aspects of an image affect the model's prediction, Grad-CAM displays class activation maps. Grad-CAM can only be used with certain models because it is unique to convolutional neural networks (CNNs).

- Why LIME Is Better: LIME can be used with any machine learning model, including YOLO for vessel segmentation, because it is model-agnostic. Conversely, Grad-CAM is restricted to CNNs and necessitates specialized architecture knowledge.

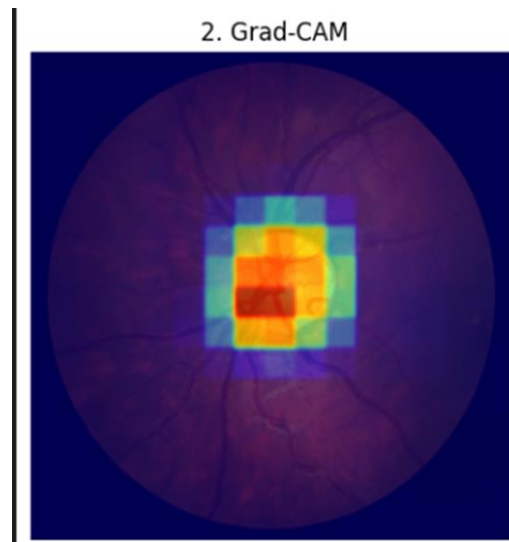


Fig 11.2 GRAD-CAM result

- A heatmap of the areas of the image that affected the model's choice is displayed in the Grad-CAM visualization for YOLO's vessel segmentation in Fig. 11.2. Compared to LIME's explanation, Grad-CAM lacks the granularity and clear explanation of specific features (such as vein structures and arterial boundaries), even though it highlights significant areas of the vessel. The picture illustrates how Grad-CAM recognizes broad areas but misses specific details within them.

## Integrated Gradients

By computing the gradients of the model's output in relation to the input features, Integrated Gradients allocates significance to the features. Although it does not offer localized explanations, it aids in comprehending how various features influence the model's decision.

- **Why LIME Is Better:** LIME offers more detailed, localized explanations, which are particularly crucial for image-based tasks like vessel segmentation where it's necessary to highlight particular areas.

### 3. Integrated Gradients

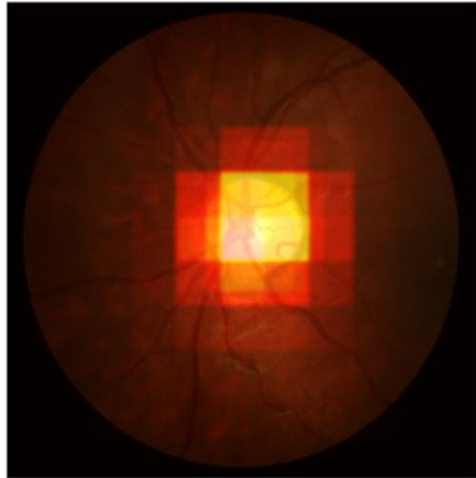


Fig 11.3 Integrated Gradients results

- Fig. 11.3's Integrated Gradients visualization provides a gradient-like overlay to illustrate the significance of each feature. In contrast to LIME's distinct region segmentation, the generated images are more difficult to understand. LIME's superpixel-based explanation offers more intuitive insights into the specific areas of the image that drive the model's prediction, whereas Integrated Gradients in the PowerPoint example provides an overall feature importance.

### **Anchors**

Anchors offer rule-based justifications, pointing out prerequisites that a model needs to make a decision. It is helpful for comprehending high-level decision rules, but it doesn't provide information about how important specific features are.

- **Why LIME is Better:** Unlike Anchors, which only tell us the features that are required for a decision, LIME provides information on both the degree of importance and whether a feature is important.



#### 4. Anchors

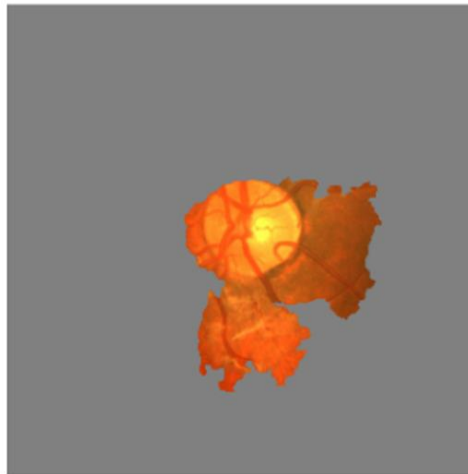


Fig 11.4 Anchors result

- The visualization of Anchors The areas that Anchors determined were essential for the decision are displayed in Fig. 11.4. But it doesn't go into detail about how much each region affects the choice. The side-by-side comparison of the Anchor and LIME outputs, Fig 12.3 on the other hand, demonstrates how LIME's image clearly highlights the particular superpixels (vessel regions) that had a greater influence.

### Counterfactual

Counterfactual explanations illustrate what would have to happen in a particular situation for the model to produce a different forecast. Although this approach lacks granularity, it aids in comprehending important factors that influence a model's decision.

- **Why LIME Is Better:** While Counterfactuals only indicate what must change for a different decision, LIME offers a more nuanced explanation by pointing out which features directly influence a model's decision and by how much.

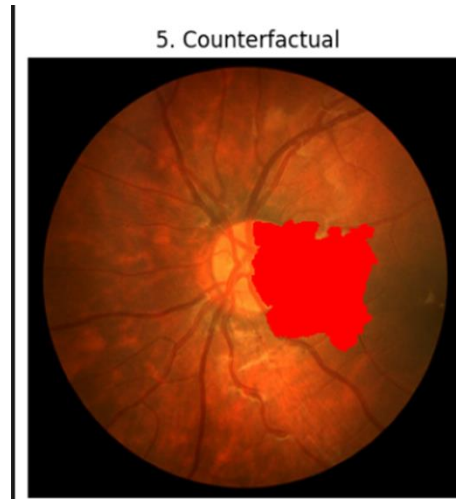


Fig 11.5 Counterfactual results

- Though it doesn't explain the significance of each feature or region, the Counterfactual visualization in Fig. 11.5 shows what changes would lead to a different decision. On the other hand, LIME's output (Fig 12.3) offers more thorough insights by clearly breaking down the vessel regions that were essential to YOLO's prediction.

### Random Masking

To determine the significance of various regions, random masking entails obstructing portions of the input (for images, this is done by masking random pixels). This approach is helpful, but it doesn't provide clear insights into the significance of features.

- **Why LIME Is Better:** Unlike Random Masking, which uses random pixel-level occlusions that might have little or no effect on the prediction, LIME disturbs meaningful regions in images by working with superpixels, making it more stable and interpretable.



Fig 11.6 Random masking

- The visualization of Random Masking Although occluded regions are randomly displayed in Fig. 11.9, the targeted perturbations observed in LIME are absent. On the other hand, LIME's explanation (displayed in a different image) makes it evident which superpixels—which correspond to the vessel's key areas—had an impact on the prediction.

## 6. Application of LIME in YOLO Model for Vessel Segmentation

A potent deep learning model for object detection, including retinal vessel segmentation, is called YOLO (You Only Look Once). Although it is not interpretable, it does a good job of detecting vessels. LIME can guarantee that the model is concentrating on significant features, like the size and shape of the vessels, rather than unimportant artifacts by providing an explanation of YOLO's predictions.

### 6.1 LIME's Perturbation Process

Superpixels, which are areas of connected pixels that depict anatomical structures, are disturbed by LIME. These superpixels represent critical regions such as the optic disk or blood vessels in retinal images. LIME shows which areas are essential for YOLO's vessel location prediction by turning off particular superpixels.

## 6.2 Visualization and Results

Visualization of LIME model outputs :



Fig 12.1 Retinal fundus image

- **Original Image:** In Fig 12.1 interprets a retinal fundus image with the optic disk and vessels.

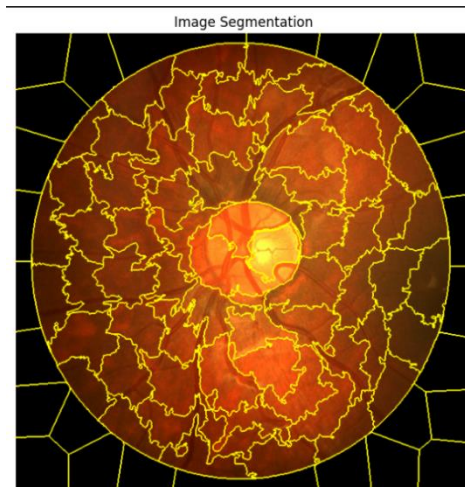


Fig 12.2 Perturbed image using LIME

- **Perturbed Image:** In Fig 12.2 The superpixels that have been turned off to test their influence on YOLO's predictions.



Fig 12.3 LIME explanation

- **LIME Explanation:** In Fig 12.3 the regions highlighted in yellow-green indicate the superpixels that significantly influence YOLO's decision. These explanations confirm that YOLO focuses on meaningful anatomical structures, providing trust in its predictions.

### 6.3 LIME Application Across Multiple Datasets

To assess the robustness of LIME in explaining YOLO's vessel segmentation predictions, we validated the method on three widely-used retinal image datasets: **DRIVE**, **CHASEDB1**, and **STARE**.

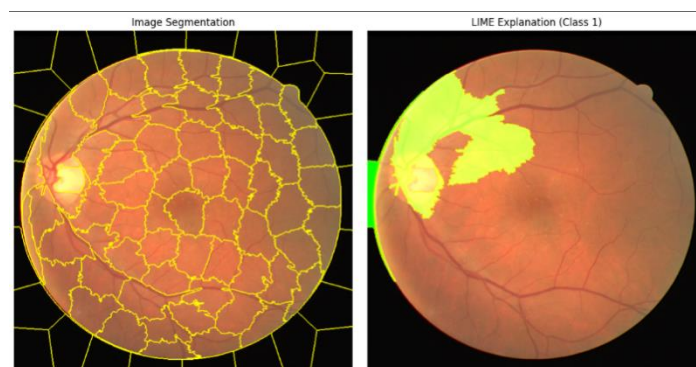


Fig 13.1 LIME explanation on Drive dataset

- **DRIVE:** In Fig 13.1 the results from LIME on the DRIVE dataset were not as robust or insightful as those from the other two datasets. This could be due to variations in the quality of the dataset, the complexity of the images, or differences in the characteristics

of the vessels in this dataset. Despite LIME providing explanations, they were less stable and didn't offer as clear a delineation of the critical vessel regions as expected.

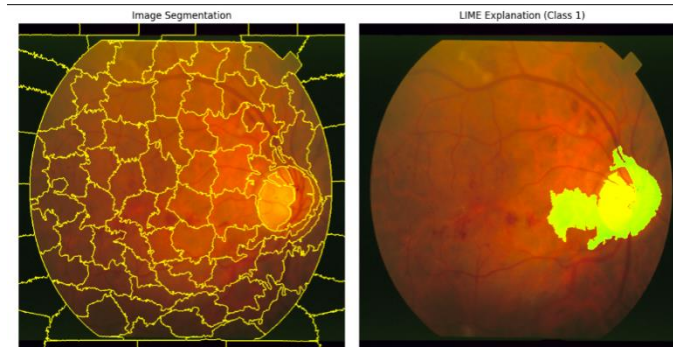


Fig 13.2 LIME explanation on Stare dataset

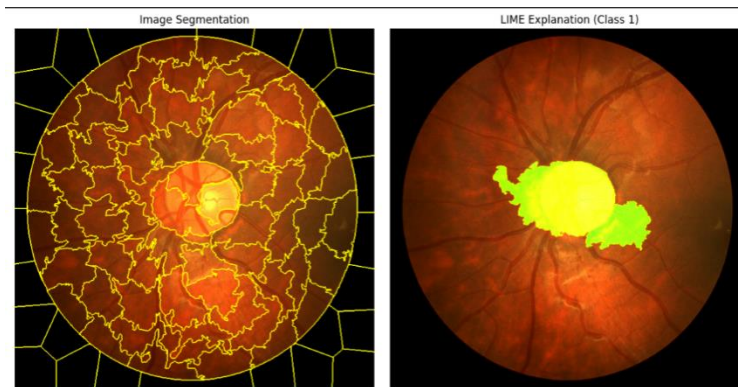


Fig 13.3 LIME explanation on Chasedb1 dataset

- **CHASEDB1 and STARE:** Conversely, the CHASEDB1 and STARE datasets produced superior outcomes. Clearly showing the areas of interest—the veins and arteries—which are vital for vessel segmentation, LIME's explanations in Fig 13.2 and Fig 13.3 were more consistent and insightful. When the dataset quality was high and the vessel structures were more visible, LIME's capacity to clarify YOLO's decision-making was shown by the significantly improved accuracy and stability of the explanations.

## 6.4 Insights and Discussion

The comparison of these three datasets demonstrates that the efficacy of LIME is contingent upon both the intrinsic properties of the dataset and the interpretability method selection. LIME produced consistent and localized explanations for CHASEDB1 (Fig. 13.3) and STARE (Fig. 13.2), but it did not produce the same level of clarity for the DRIVE dataset. This might be the result of issues with noise, image quality, or the DRIVE dataset's lack of as many distinguishing features as STARE and CHASEDB1.

These findings imply that the efficacy of LIME may differ based on the intrinsic characteristics of the dataset, and future studies may examine ways to optimize or modify LIME's use for datasets with poorer quality or less distinct vessel structures.

## **7. Conclusion**

The best interpretability technique for YOLO-based vessel segmentation tasks turns out to be LIME. It is a priceless tool for comprehending the predictions of intricate models because of its model-agnostic nature, local explainability, and capacity to highlight significant areas in images. LIME is the best option for this study due to its flexibility, clarity, and granularity in describing particular predictions, even though other interpretability techniques like SHAP and Grad-CAM have advantages as well.

## CHAPTER 12

### Rule-Based Classification for CVD Risk Assessment

#### 12.1 Introduction to Rule-Based Classification

Here, we present the rule-based classification framework intended for Cardiovascular Disease (CVD) Risk Assessment based on retinal biomarkers. Unlike machine learning models that need a large amount of labeled data, rule-based classification offers an interpretable and deterministic method based on pre-defined conditions from medical expertise. Our framework combines multiple ophthalmic biomarkers (OBM) and vessel-based measures like Artery-to-Vein Ratio (AVR), Cup-to-Disc Ratio (CDR), and Fractal Dimension (FD) to classify individuals into high or low-risk groups.

#### 12.2 Rule-Based Classification Algorithm

The classification system follows a stepwise decision-making process to determine CVD risk.

##### Step 1: Define Ophthalmic Biomarkers (OBM)

High-risk ophthalmic biomarkers include retinal abnormalities strongly associated with cardiovascular conditions. The presence of any of these biomarkers is a direct indicator of high CVD risk, as expressed in **Equation (12.1)**:

$$OBM = BDR \cup PDR \cup CNV \cup ASR \cup HR \cup CRVO \cup BRVO \cup HCRVO \cup CRAO \cup BRAO \cup MA \quad (12.1)$$

##### Step 2: Define AVR Condition

Artery-to-Vein Ratio (AVR) is a key vascular parameter, with values outside the **normal range (0.67 - 0.75)** indicating potential cardiovascular risk. The condition is mathematically defined in **Equation (12.2)**:

$$AV_{Flag} = \begin{cases} 1, & \text{if } AVR < 0.67 \text{ or } AVR > 0.75 \\ 0, & \text{otherwise} \end{cases} \quad (12.2)$$

##### Step 3: Define CDR Condition

Cup-to-Disc Ratio (CDR) helps assess optic disc morphology. A **CDR greater than 0.6** suggests a possible underlying health issue, as shown in **Equation (12.3)**:



$$CDR_{Flag} = \begin{cases} 1, & \text{if } CDR > 0.6 \\ 0, & \text{otherwise} \end{cases} \quad (12.3)$$

#### Step 4: Define Fractal Dimension (FD) Condition

Fractal Dimension (FD) measures the complexity of the vascular structure. An **FD value below 1.3** suggests vessel abnormalities related to cardiovascular risks. The condition is mathematically described in **Equation (12.4)**:

$$FD_{Flag} = \begin{cases} 1, & \text{if } FD < 1.3 \\ 0, & \text{otherwise} \end{cases} \quad (12.4)$$

#### Step 5: Define Neutral Biomarkers (NBM)

Neutral biomarkers are retinal conditions that do not directly indicate cardiovascular issues but may still be present. The set of neutral biomarkers is defined in **Equation (12.5)**:

$$NBM = Normal \cup Coat - Disease \cup Drusen \quad (12.5)$$

#### Step 6: Compute CVD Risk Based on Conditions

The final classification follows specific decision rules:

##### *Rule 1: Direct High-Risk Condition*

If an individual has any high-risk **ophthalmic biomarker (OBM)**, they are classified as **high risk**, as per **Equation (12.6)**:

$$\text{if } OBM = 1, CVD_{Risk} = 1 \quad (12.6)$$

##### *Rule 2: Normal Features + Only Neutral Biomarkers → Low Risk*

If no abnormalities exist and only **neutral biomarkers** are present, the individual is classified as **low risk**, as given in **Equation (12.7)**:

$$\text{if } (NBM = 1) \text{ and } (AVR, CDR, FD \text{ are normal}), \text{ then } CVD_{Risk} = 0 \quad (12.7)$$

##### *Rule 3: Neutral Biomarkers + Abnormal Retinal Features → High Risk*

If an individual has neutral biomarkers but exhibits any **abnormal retinal feature**, they are classified as **high risk**, as described in **Equation (12.8)**:

*if* ( $NBM = 1$ ) *and* ( $AV_{Flag} = 1 \cup CDR_{Flag} = 1 \cup FD_{Flag} = 1$ ), *then*  $CVD_{Risk} = 1$   
( 12.8)

#### **Rule 4: No Neutral Biomarkers + Any Abnormal Feature → High Risk**

If an individual has no neutral biomarkers and **any** of the abnormal features, they are classified as **high risk**, as shown in **Equation (12.9)**:

*if* ( $NBM = 0$ ) *and* ( $AV_{Flag} = 1 \cup CDR_{Flag} = 1 \cup FD_{Flag} = 1$ ), *then*  $CVD_{Risk} = 1$   
(12.9)

### **Final Decision Rule**

#### **Advantages of Rule-Based Classification**

The rule-based system has a number of benefits compared to intricate machine-learning models. To begin with, it supports interpretability and enables clinicians to comprehend why one classification is issued over another. In contrast to deep learning models that need considerable training data, this method is data-efficient and can be easily applied to actual clinical situations. Moreover, by drawing on established medical criteria, it maintains the decision-making process in accordance with clinical best practices and, therefore, is a strong solution to undertake early cardiovascular disease risk assessment based on retinal biomarkers.

## CONCLUSION

This work presents a cardiovascular disease (CVD) risk estimation framework that utilizes retinal fundus images for non-invasive screening. By integrating vascular, structural, and fractal biomarkers, the proposed method significantly enhances the accuracy of CVD risk detection. The key biomarkers used in this framework include Arteriovenous Ratio (AVR), Cup-to-Disc Ratio (CDR), Fractal Dimension (FD), and ophthalmic biomarkers, which collectively provide a comprehensive assessment of retinal vascular health.

This study highlights the potential of retinal imaging in preventive healthcare, offering a cost-effective and efficient alternative for large-scale CVD risk assessment. With future advancements, including automated feature extraction and real-time analysis, this framework can further enhance early diagnosis and intervention, contributing to improved cardiovascular health monitoring and disease prevention.

## FUTURE WORK

In this research, we have developed and thoroughly evaluated a cardiovascular disease (CVD) risk prediction system based on retinal image analysis. Retinal imaging has emerged as a promising non-invasive diagnostic tool for assessing systemic vascular health, as the microvascular structures in the retina closely reflect broader cardiovascular conditions. By analyzing key vascular and structural features, our system aims to provide an early risk assessment for individuals who may be at a higher risk of developing CVD.

Our approach integrates multiple critical retinal biomarkers, including Arteriovenous Ratio (AVR), Cup-to-Disc Ratio (CDR), and Fractal Dimension (FD), alongside ophthalmic biomarkers that indicate disease-related abnormalities. The AVR provides insights into the relative widths of arteries and veins, which is crucial for detecting vascular narrowing and hypertension-related changes. The CDR helps assess structural deformations in the optic nerve head, which are often associated with glaucoma and increased intracranial pressure—factors that can also correlate with cardiovascular risk.

Currently, our system relies on manually extracted ophthalmic biomarkers, which require prior segmentation and classification of retinal structures before feeding the extracted features into the prediction model. While this approach has demonstrated high accuracy and reliability, it comes with a significant limitation—the dependency on manual annotation and expert intervention. A key area of future research is the development of an automated feature extraction method capable of identifying and quantifying ophthalmic biomarkers directly from raw retinal images without requiring human intervention. This could be achieved by leveraging advanced deep learning models such as convolutional neural networks (CNNs), transformer-based architectures, or graph-based learning techniques. Automating the feature extraction process would significantly enhance the scalability and clinical applicability of our system, allowing for real-time CVD risk assessment in large-scale screening programs. By eliminating manual feature extraction and integrating an end-to-end deep learning framework, future iterations of this system could improve efficiency,

reduce costs, and enable early disease detection with minimal human supervision. This advancement would further strengthen the role of retinal imaging as a powerful, non-invasive biomarker for cardiovascular risk assessment, ultimately leading to better preventive healthcare strategies and early intervention protocols.

## **REFERENCES**

- [1]World Health Organization (WHO), "Cardiovascular diseases (CVDs)," [Online]. Available: <https://www.who.int>. [Accessed: Oct. 10, 2023].
- [2]Rudnicka AR, Welikala R, Barman S, et al., "Artificial intelligence-enabled retinal vasculometry for prediction of circulatory mortality, myocardial infarction and stroke," *British Journal of Ophthalmology*, vol. 106, pp. 1722–1729, 2022.
- [3]Sandoval-Garcia, E., McLachlan, S., Price, A.H. et al., "Retinal arteriolar tortuosity and fractal dimension are associated with long-term cardiovascular outcomes in people with type 2 diabetes," *Diabetologia*, vol. 64, pp. 2215–2227, 2021. <https://doi.org/10.1007/s00125-021-05499-z>.
- [4]Singh C., "Metabolism and Vascular Retinopathies: Current Perspectives and Future Directions," *Diagnostics (Basel)*, vol. 12, no. 4, p. 903, 2022. DOI: 10.3390/diagnostics12040903.
- [5]M. Kiruthika et al., "Artery and Vein Classification for Hypertensive Retinopathy," in *Proc. IEEE ICOEI*, 2019, pp. 244–248. DOI: 10.1109/ICOEI.2019.8862719.
- [6]S. Dinesen et al., "Retinal Vascular Fractal Dimensions and Their Association with Macrovascular Cardiac Disease," *Ophthalmic Res.*, vol. 64, no. 4, pp. 561–566, 2021. DOI: 10.1159/000514442.
- [7]Ehrlich JR, Kaluzny M, Baumann S, Lehmann R, Hohnloser SH, "Biomarkers of structural remodelling and endothelial dysfunction for prediction of cardiovascular events or death in patients with atrial fibrillation," *Clin Res Cardiol*, vol. 100, no. 11, pp. 1029–1036, 2011. DOI: 10.1007/s00392-011-0337-9.
- [8] T. Y. Wong et al., "Retinal arteriolar narrowing and risk of coronary heart disease," *Circulation*, vol. 121, no. 2, pp. 248–254, 2010.
- [9] M. K. Ikram et al., "Retinal vessel caliber and risk of stroke," *Neurology*, vol. 81, no. 11, pp. 983–990, 2013.
- [10] K. Poplin et al., "Predicting cardiovascular risk factors from retinal fundus photographs," *Nature Biomed. Eng.*, vol. 2, pp. 158–164, 2018.
- [11] Y. Zheng et al., "Ophthalmomomics for CVD risk stratification," *IEEE JBHI*, vol. 25, no. 5, pp. 1725–1734, 2021.
- [12] A. D. Hughes et al., "Prospective validation of retinal CVD biomarkers," *Eur. Heart J.*, vol. 42, no. 10, pp. 1012–1023, 2021.
- [13] R. Kawasaki et al., "Global generalizability of retinal CVD models," *Lancet Digit. Health*, vol. 4, no. 1, pp. e51–e62, 2022.

- [14] J. Moura et al., "Deep learning of retinal vasculature for CVD risk," *IEEE TMI*, vol. 40, no. 4, pp. 1090–1101, 2021.
- [15] S. R. Sadda et al., "Additive value of retinal biomarkers for CVD prediction," *JAMA Cardio.*, vol. 6, no. 5, pp. 532–540, 2021.
- [16] R. Krishnan, V. Sekhar, J. Sidharth, S. Gautham, and G. Gopakumar, "Glaucoma detection from retinal fundus images," 2020 International Conference on Communication and Signal Processing (ICCSP), 2020.
- [17] K. P. Shah, S. N. Sah, O. Kothari, T. Singh, and P. Patra, "Diabetic retinopathy using OCT images," 2024 15th International Conference on Computing Communication and Networking Technologies (ICCCNT), Kamand, India, 2024, pp. 1–6.
- [18] S. Kanakaprabha, D. Radha, and S. Santhanalakshmi, "Diabetic retinopathy detection using deep learning models," in *Ubiquitous Intelligent Systems. ICUIS 2021. Smart Innovation, Systems and Technologies*, vol. 302, P. Karuppusamy, F. P. García Márquez, and T. N. Nguyen, Eds. Springer, Singapore, 2022.

#### Vessel segmentation literature survey:

- [19] N. Lv, L. Xu, Y. Chen, W. Sun, J. Tian, and S. Zhang, "TCDDU-Net: Combining Transformer and Convolutional Dual-Path Decoding U-Net for Retinal Vessel Segmentation," *Scientific Reports*, vol. 14, no. 1, 2024, Art. no. 77464. doi: 10.1038/s41598-024-77464-w.
- [20] H. Cao, Y. Wang, J. Chen, D. Jiang, X. Zhang, Q. Tian, and M. Wang, "Swin-Unet: Unet-like Pure Transformer for Medical Image Segmentation," *arXiv preprint arXiv:2105.05537*, May 2021. [Online].

#### AV literature survey :

- [21] R. Estrada et al., "Automatic retinal artery and vein classification via deep learning," *IEEE Trans. Med. Imaging*, vol. 35, no. 11, pp. 2364-2374, 2016.
- [22] Y. Guo et al., "RRWNet: Recursive refinement network for artery-vein segmentation," *IEEE Trans. Med. Imaging*, vol. 41, no. 8, pp. 1976-1988, 2022.
- [23] T. Son et al., "Dynamic vessel segmentation for hypertensive retinopathy," *IEEE JBHI*, vol. 26, no. 5, pp. 2354-2365, 2022.
- [24] B. Dashtbozorg et al., "Automatic AVR measurement," *IEEE JBHI*, vol. 23, no. 3, pp. 1247-1258, 2019.
- [25] K. Poplin et al., "CVD risk prediction from fundus images," *Nature Biomed. Eng.*, vol. 2, no. 3, pp. 158-164, 2018.

- [26] J. Moura et al., "Multi-biomarker retinal analysis," *IEEE Access*, vol. 9, pp. 68941-68953, 2021.
- [27] A. Rani and D. Mittal, "Measurement of Arterio-Venous Ratio for Detection of Hypertensive Retinopathy through Digital Color Fundus Images," *Journal of Biomedical Engineering and Medical Imaging*, vol. 2, no. 5, pp. 35-45, 2015. DOI: 10.14738/jbemi.25.1577.
- [28] R. Manjunatha and H. S. Sheshadri, "Boundary Extraction and Vessel Width Calculation in Retinal Fundus Images," *Asian Journal of Engineering and Applied Technology*, vol. 8, no. 2, pp. 63-70, 2019.
- [29] M. Kiruthika, T. R. Swapna, C. Kumar, and K. P. Peeyush, "Artery and Vein Classification for Hypertensive Retinopathy," *Proc. IEEE ICOEI*, 2019, pp. 244-248. DOI: 10.1109/ICOEI.2019.8862719.
- [30] T. Y. Wong et al., "Retinal Arteriolar Narrowing and Risk of Hypertension and Stroke," *Circulation*, vol. 106, no. 8, pp. 963-969, 2002.
- [31] A. R. Sharrett et al., "Atherosclerosis Risk in Communities Study: Retinal Arteriolar Narrowing and Cardiovascular Mortality," *Stroke*, vol. 34, no. 2, pp. 411-416, 2003.
- [32] Hu Cao, Yueyue Wang, Joy Chen, Dongsheng Jiang, Xiaopeng Zhang, Qi Tian, and Manning Wang. 2022. Swin-Unet: Unet-Like Pure Transformer for Medical Image Segmentation. In *Computer Vision – ECCV 2022 Workshops: Tel Aviv, Israel, October 23–27, 2022, Proceedings, Part III*. Springer-Verlag, Berlin, Heidelberg, 205–218.
- Cup-Disc Ratio Literature Survey:
- [33] Chen, N., Lv, X. Research on segmentation model of optic disc and optic cup in fundus. *BMC Ophthalmol* **24**, 273 (2024).
- Ophthalmic Biomarkers Literature Survey:
- [34] Grunwald JE, Pistilli M, Ying GS, Maguire MG, Daniel E, Whittock-Martin R, Parker-Ostroff C, Jacoby D, Go AS, Townsend RR, Gadegbeku CA, Lash JP, Fink JC, Rahman M, Feldman H, Kusek JW, Xie D; CRIC Study investigators. Progression of retinopathy and incidence of cardiovascular disease: findings from the Chronic Renal Insufficiency Cohort Study. *Br J Ophthalmol*.
- [35] Yu W, Yang B, Xu S, Gao Y, Huang Y, Wang Z. Diabetic Retinopathy and Cardiovascular Disease: A Literature Review. *Diabetes Metab Syndr Obes*. 2023 Dec 28;16:4247-4261.
- [36] Liew G, Xie J, Nguyen H, Keay L, Kamran Ikram M, McGeechan K, Klein BE, Jin Wang J, Mitchell P, Klaver CC, Lamoureux EL, Wong TY. Hypertensive retinopathy and cardiovascular disease risk: 6 population-based cohorts meta-analysis.



[37] Colcombe J, Munda R, Kaiser A, Bijon J, Modi Y. Retinal Findings and Cardiovascular Risk: Prognostic Conditions, Novel Biomarkers, and Emerging Image Analysis Techniques. *J Pers Med*. 2023 Oct 31;13(11):1564

#### Fractal dimension literature survey

[38] N. Cheung, M. Islam, B. Thiagalingam, P. Mitchell, and T. Y. Wong, "Traditional and Novel Cardiovascular Risk Factors for Retinal Vein Occlusion: The Multiethnic Study of Atherosclerosis," *Ophthalmology*, vol. 114, no. 1, pp. 86–92, 2007.

[39] Sandoval-Garcia et al., "Study on Retinal Vascular Complexity and Health Prediction."

[40] H. Jelinek, M. E. Fernandez, and P. G. T. Howell, "Neurons and Fractals: How Reliable and Useful Are Calculations of Fractal Dimension?" *Frontiers in Physiology*, vol. 9, p. 1516, 2018.

[41] T. Kawasaki, Y. Zhang, P. J. Huynh, R. H. Silverman, and J. S. Schuman, "Fractal Dimension of the Retinal Vasculature and Risk of Stroke," *Stroke*, vol. 42, no. 7, pp. 1821–1828, 2011.

[42] Y. T. Ong, G. Hilal, M. H. Cheung, C. M. Venketasubramanian, and J. C. Ng, "Microvascular Structure and Network in the Retina of Patients With Ischemic Stroke," *Stroke*, vol. 44, no. 8, pp. 2121–2127, 2013.

[43] M. Luppe, "Fractal Dimension Based on Minkowski-Bouligand Method Using Exponential Dilations," *Applied Mathematics and Computation*, vol. 250, pp. 60–72, 2015.

[44] G. Liew, J. J. Wang, P. Mitchell, and T. Y. Wong, "Retinal Vasculature Fractal and Stroke Mortality," *Stroke*, vol. 52, no. 2, pp. 123–130, 2021.

[45] J. Cheeseman and E. R. Vrscay, "Estimating the Fractal Dimensions of Vascular Networks and Other Branching Structures: Some Words of Caution," *Mathematical Biosciences and Engineering*, vol. 19, no. 1, pp. 451–468, 2022.

[46] A. W. Setiawan, T. R. Mengko, O. S. Santoso and A. B. Suksmono, "Color retinal image enhancement using CLAHE," *International Conference on ICT for Smart Society*, Jakarta, Indonesia, 2013, pp. 1-3, doi: 10.1109/ICTSS.2013.6588092. keywords: {Retina;Image color analysis;Image enhancement;Colored noise;Biomedical imaging;Image quality;Blood vessels;color;retinal image;asymmetric;enhancement;CLAHE},

[47] Erwin, R. Zulfahmi, D. S. Noviyanti, G. R. Utami, A. N. Harison and P. S. Agung, "Improved Image Quality Retinal Fundus with Contrast Limited Adaptive Histogram Equalization and Filter Variation," *2019 International Conference on Informatics, Multimedia, Cyber and Information System (ICIMCIS)*, Jakarta, Indonesia, 2019, pp. 49-54, doi:

10.1109/ICIMCIS48181.2019.8985198. keywords: {Enhancement;CLAHE;Median Filter;Wiener Filter;Gaussian Filter},

- [48] W. Chen, J. Zhang, Y. Zhang, and W. Chen, "TW-GAN: Topology and width aware GAN for retinal artery/vein classification," *Med. Image Anal.*, vol. 77, p. 102340, 2022.
- [49] F. Girard, C. Kavalec, F. Cheriet, and D. Lesage, "A joint segmentation and classification framework for retinal arteries and veins," *IEEE Trans. Med. Imaging*, vol. 38, no. 2, pp. 438–448, 2019.
- [50] E. Kang, J. Min, and J. C. Ye, "A deep convolutional neural network using directional wavelets for low-dose X-ray CT reconstruction," *Med. Phys.*, vol. 44, no. 10, pp. e360–e375, 2020.
- [51] Q. Hu, M. D. Abràmoff, and M. K. Garvin, "Automated separation of binary overlapping trees in low-contrast color retinal images," in *Proc. Med. Image Comput. Comput.-Assist. Interv. (MICCAI)*, 2013, pp. 436–443.
- [52] J. Morano, G. Aresta, and H. Bogunović, "RRWNet: Recursive Refinement Network for Effective Retinal Artery/Vein Segmentation and Classification," *Expert Syst. Appl.*, vol. 256, p. 124970, 2024.
- [53] O. Ronneberger, P. Fischer, and T. Brox, "U-Net: Convolutional networks for biomedical image segmentation," in *Proc. Med. Image Comput. Comput.-Assist. Interv. (MICCAI)*, 2015, pp. 234–241.
- [54] Z. Zhou, M. M. R. Siddiquee, N. Tajbakhsh, and J. Liang, "UNet++: Redesigning skip connections to exploit multiscale features in image segmentation," *IEEE Trans. Med. Imaging*, vol. 39, no. 6, pp. 1856–1867, 2020.
- [55] O. Oktay et al., "Attention U-Net: Learning where to look for the pancreas," in *Proc. Med. Image Comput. Comput.-Assist. Interv. (MICCAI)*, 2018, pp. 605–612.